

VSOP SPACE VLBI AND GEODETIC VLBI INVESTIGATIONS OF SOUTHERN HEMISPHERE RADIO SOURCES

S. J. TINGAY¹

CSIRO Australia Telescope National Facility, Paul Wild Observatory, Narrabri, NSW 2390, Australia;
Steven.Tingay@csiro.au

J. E. REYNOLDS, A. K. TZIOMIS, DAVID L. JAUNCEY, AND J. E. J. LOVELL
CSIRO Australia Telescope National Facility, P.O. Box 76, Epping, NSW 2121, Australia

R. DODSON, M. E. COSTA, AND P. M. MCCULLOCH
Department of Physics, University of Tasmania, G.P.O. Box 252-21, Hobart, Tasmania 7001, Australia

P. G. EDWARDS AND H. HIRABAYASHI
Institute of Space and Astronautical Science, Sagami-hara, Kanagawa 229, Japan

D. W. MURPHY AND R. A. PRESTON
Jet Propulsion Laboratory, California Institute of Technology, MS 238-332, 4800 Oak Grove Drive, Pasadena, CA 91109

B. G. PINER
Whittier College, Department of Physics, 13406 Philadelphia Street, Whittier, CA 90608

G. D. NICOLSON AND J. F. H. QUICK
Hartebeesthoek Radio Astronomy Observatory, P.O. Box 443, Krugersdorp 1740, Transval, South Africa

AND

H. KOBAYASHI AND K. M. SHIBATA
National Astronomical Observatory of Japan, Mitaka, Tokyo 181-8588, Japan

Received 2002 January 7; accepted 2002 March 19

ABSTRACT

We present images from VLBI Space Observatory Programme (VSOP) observations of 14 compact extragalactic southern hemisphere radio sources, including a description of the observations, the data reduction techniques, and the parameters of the resulting images and model fits. These images provide the highest resolution information to date for many of these objects. Comparisons are made between VSOP and previous ground-based VLBI results, including images from data extracted from the geodetic VLBI archive at the United States Naval Observatory. From the VSOP data, we find that the two radio galaxies observed have lower peak brightness temperatures than the 12 quasars. Also, these data show (1) no evidence for obvious differences between the brightness temperature distributions of gamma-ray-loud and gamma-ray-quiet radio-loud active galactic nuclei and (2) no evidence for obvious correlations between brightness temperature and spectral index, radio polarization, flux density, or month timescale modulation index. These results are consistent with previous work by Lister, Tingay, & Preston, who found that the only observable significantly correlated with VSOP-derived brightness temperature is intraday variability, which is strongly correlated with many relativistic beaming indicators. For one source, PKS 1127–145, we undertake a detailed investigation of the milliarcsecond-scale component positions as a function of time, taking data from the literature and the current work, to estimate proper motions. As a result, we suggest that two components previously reported as stationary, C1 and C2, have apparent transverse speeds of (9.1 ± 3.8) and $(5.3 \pm 2.3) h^{-1}c$, respectively. We also make the first investigation of the apparent motion in the nearest GHz-peaked spectrum radio galaxy, PKS 1718–649, finding an upper limit on the apparent separation speed of $0.08c$. Comparison of geodetic VLBI and VSOP data show no significant detection of component motion in PKS 0208–512, $(2.4 \pm 3.1) h^{-1}c$, and only a tentative detection in PKS 0537–441, $(2.8 \pm 2.2) h^{-1}c$. A significant detection of component motion is found in PKS 1610–771, solely from the geodetic VLBI data, $(9.4 \pm 3.5) h^{-1}c$.

Subject headings: galaxies: active — galaxies: jets — quasars: general —
radiation mechanisms: nonthermal — radio continuum: galaxies —
techniques: interferometric

1. INTRODUCTION

The VLBI Space Observatory Programme (VSOP) is led by the Japanese Institute of Space and Astronautical Science (ISAS) and relies upon the coordinated effort of

many organizations and individuals. ISAS successfully launched the first dedicated space-based Very Long Baseline Interferometry (VLBI) radio telescope, named HALCA (Highly Advanced Laboratory for Communications and Astronomy), into Earth orbit on 1997 February 12. Since that time HALCA has observed many compact extragalactic radio sources, mainly active galactic nuclei (AGNs), supported by ground arrays such as the Very Long Baseline Array (VLBA), the European VLBI Network (EVN), and

¹ Also Jet Propulsion Laboratory, California Institute of Technology, MS 238-332, 4800 Oak Grove Drive, Pasadena, CA 91109.

the Southern Hemisphere Long Baseline Array (LBA). The HALCA orbit is such that the longest baseline formed in combination with these ground telescopes is approximately 2.6 times the diameter of the Earth, providing a corresponding resolution increase beyond the maximum possible from the ground alone, in the VSOP bands at 6 and 20 cm. A major justification for space VLBI is that the maximum brightness temperature an interferometer can measure accurately is proportional to the physical (projected) baseline length squared. Thus, VSOP has the potential to measure brightness temperatures up to 6–7 times greater than an Earth-based interferometer. Full descriptions of the VSOP mission can be found in Hirabayashi et al. (1998, 2000a).

We have used the VSOP mission facilities to observe compact extragalactic radio sources at southern declinations, as the logical extension to ground-based investigations that have taken place over the last 10 yr (Tingay et al. 1996a, 1996b, 1997, 1996a, 1998b, 1998c, 2000; Tornikoski et al. 1999). Sources of various AGN classes have been observed as part of this work, corresponding to several separate proposals to the VSOP mission submitted during the first two announcement of opportunity (AO) periods (1997–1999). The proposals include the following: gamma-ray-loud and gamma-ray-quiet AGNs with VSOP and SHEVE at 5 GHz (V115, AO1), VSOP and the bursting gamma-ray source PKS 2255–282 (W025, AO2), continuous monitoring of ecliptic pole source PKS 0637–752 (W029, AO2), gamma-ray-loud and gamma-ray-quiet AGNs with VSOP at 5 GHz (W030, AO2), and high linear resolution imaging of $z < 0.06$ sources (W062, AO2).

Gamma-ray-loud sources for V115 were selected to be those south of declination $\delta = -40^\circ$ in the first Energetic Gamma Ray Experiment Telescope (EGRET) catalog (Fichtel et al. 1994). The V115 gamma-ray quiet sources were selected to be south of $\delta = -40^\circ$, EGRET nondetections according to Fichtel et al. (1994) and have radio (flux density and spectral index) and optical properties (polarization) that are typical of the gamma-ray-loud radio source population. The additional sources selected for W030 were selected on the same basis, except that the declination limit for the gamma-ray-loud sources was raised to $\delta = -10^\circ$, to include more sources. Also, over the years since the analysis of Fichtel et al. (1994), the EGRET source list has been modified, with the result that some of the originally selected sources have switched categories. For the work in this paper we use the identifications given in the most recent EGRET catalog, that of Hartman et al. (1999). The gamma-ray source PKS 2255–282 was selected individually as an interesting single source because of the gamma-ray and millimeter flares that brought it to prominence (Tornikoski et al. 1999).

The low-redshift sources were selected from the list of 1 Jy sources at 5 GHz (and $|b| > 10^\circ$) of Stickel, Meisenheimer, & Kühr (1994); of 527 sources, 71 lie at redshifts less than $z = 0.06$, yielding 1 mas \equiv 1 pc. From the 71 sources we took 29 as candidate sources for our sample (those with flat radio spectra and those with total flux densities greater than 4 Jy). We searched the literature for these sources and found that 12 of these contain in excess of 1 Jy on moderate length VLBI baselines (for example, baselines within Australia). For observation from the southern hemisphere, we selected six of these sources, those south of $\delta = 0^\circ$.

A total of 14 sources have been observed as part of these projects. We present the VSOP results for all of these

observations together in this paper, since in all cases the observational and data reduction techniques are very similar. Also presented are new results for some of these sources based on geodetic VLBI data. We derive and discuss basic parameters of the sources and the samples. Subsequent papers will deal with the detailed statistical interpretation of the data for the various classes of source, drawing from the current VLBI and radio data and the wider literature.

The VSOP images presented here represent the highest angular resolution images ever obtained for the majority of these radio sources. Throughout this paper $q_0 = 0.1$ has been used, unless stated otherwise.

2. OBSERVATIONS, DATA REDUCTION, AND RESULTS

2.1. VSOP Data

Table 1 lists the sources observed by the VSOP mission, the appropriate observing proposal, as listed above, and basic data such as average 4.8 GHz flux density, average spectral index between 4.8 and 8.6 GHz, average percentage polarization at 4.8 GHz, redshift, and object identification. The flux density, spectral index, and polarization data are averages obtained from Australia Telescope Compact Array (ATCA) monitoring observations between 1996 July and 2000 February, using the 6 km maximum baseline of the ATCA (S. J. Tingay et al. 2002, in preparation). Also given in Table 1 are the rms deviations from the mean flux density at 4.8 GHz observed between 1996 and 2000 and the ratio of rms deviation to mean flux density (modulation index), derived from the ATCA data. ATCA data for PKS 1127–145 and PKS 2152–699 are not available. Data for these two sources in Table 1 are from Stickel et al. (1994).

A total of 15 successful VSOP observations of 14 sources have been made from a list of 24 sources proposed. A small number of scheduled observations were unsuccessful and may be rescheduled in the future. However, at the time of writing it appears unlikely that observations of a significant number of the remaining 10 sources will be obtained before the end of the VSOP mission, owing to tightened observing constraints for the spacecraft. Table 2 gives details of the observations for each source, including the UT date of observation, the array of ground radio telescopes used, the tracking station(s) used to track HALCA, the correlator where the data were initially processed, the frequency of observation, and the approximate time spent on-source for the ground antennas and the space antenna. The on-source time refers to the successfully correlated and fringe-fitted time ranges. Some amount of data is lost during imaging—the data that do not fulfil self-calibration requirements—and thus the time range of data finally represented in the images and (u, v) coverages may be different from those given in Table 2. All observations used a 32 MHz bandwidth, split into two 16 MHz channels; the frequency of observation is given as the center of the 32 MHz band.

Data processed at the Dominion Radio Astrophysical Observatory (DRAO) correlator in Penticton, Canada, were recorded on S2 format tapes, at both the ground telescopes and tracking stations. Data processed at the National Radio Astronomy Observatory (NRAO) VLBA correlator in Socorro, New Mexico, were recorded on VLBA format tapes. Occasionally non-NRAO telescopes not equipped with a VLBA format recording terminal

TABLE 1
SOURCES OBSERVED BY THE VSOP MISSION

Source	VSOP Experiment	$S_{4.8\text{ GHz}}$	$\alpha_{4.8}^{8.6}$	m_p	σ_{rms}	$\sigma_{\text{rms}}/S_{4.8\text{ GHz}}$	z	ID
PKS 0208–512.....	V115	3.0	–0.12	1.4	0.23	0.08	1.003	QG
PKS 0438–436.....	V115	3.2	0.10	0.6	0.32	0.11	2.852	Q
PKS 0537–441.....	V115	3.4	0.12	1.3	1.0	0.29	0.894	QG
PKS 0637–752.....	V115/W029	6.3	–0.11	1.2	0.12	0.02	0.651	Q
PKS 1104–445.....	W030	2.6	–0.05	2.4	0.23	0.10	1.598	Q
PKS 1127–145.....	W030	5.5	–1.03	1.187	Q
PKS 1424–418.....	W030	5.0	0.24	2.7	0.17	0.04	1.522	QG
PKS 1610–771.....	W030	3.0	–0.24	3.6	0.16	0.06	1.710	Q
PKS 1622–253.....	W030	1.8	0.17	1.2	0.47	0.27	0.786	QG
PKS 1622–297.....	W030	2.4	0.17	4.6	0.32	0.13	0.815	QG
PKS 1718–649.....	W062	4.6	–0.38	<0.2	0.07	0.02	0.014	GPS
PKS 2152–699.....	W062	12.3	–1.44	0.028	FRII
PKS 2255–282.....	W025	3.4	0.90	0.33	0.9	0.26	0.926	QG
PKS 2355–534.....	V115	1.5	0.09	3.1	0.03	0.05	1.006	Q

NOTE.—Source: Parkes catalog designation; $S_{4.8\text{ GHz}}$: average flux density at 4.8 GHz on the 6 km ATCA baseline in Jy, between 1996 July and 2000 February; $\alpha_{4.8}^{8.6}$: average spectral index between 4.8 and 8.6 GHz ($S \propto \nu^\alpha$) from ATCA 6 km data; m_p : average percentage linear polarization at 4.8 GHz from ATCA 6 km data; σ_{rms} : rms deviation of 4.8 GHz flux density around $S_{4.8\text{ GHz}}$, in Jy, from ATCA 6 km data; $\sigma_{\text{rms}}/S_{4.8\text{ GHz}}$: ratio of σ_{rms} to $S_{4.8\text{ GHz}}$; z : redshift; and ID: gamma-ray-quiet quasar (Q), gamma-ray-loud quasar (QG), Fanaroff-Riley type II radio galaxy (FRII), and GHz-peaked spectrum (GPS) galaxy.

recorded data on S2 format tapes and shipped them to the S2 to VLBA format translation machine at the National Astronomical Observatory of Japan (NAOJ) in Mitaka, Japan. The translated tapes were then correlated with VLBA format tapes recorded at other telescopes. Data processed at the NAOJ correlator in Mitaka were recorded on S2 format tapes and translated at Mitaka into the VSOP format used at the Mitaka correlator.

After correlation, the data were imported into the Astronomical Image Processing Software (AIPS) for further processing. The data were initially sorted into time-baseline

order using the task MSORT and then indexed using INDXR. For data from the VLBA and Mitaka correlators, the task ACCOR was used to correct the correlated amplitudes for errors in the sampler thresholds.

Calibration information for the telescopes, in the form of system temperatures and antenna gains, were collected from the participating observatories. For data from all correlators, the calibration information was loaded into AIPS using the task ANTAB and amplitude calibration tables were produced using APCAL. For the data from later observations using the VLBA, calibration information for

TABLE 2
DETAILS OF THE OBSERVATIONS FOR EACH SOURCE

SOURCE	UT DATE	GROUND TELESCOPES	TRACKING STATIONS	CORRELATOR	ν (GHz)	TIME (hr)	
						Ground	Space
PKS 0208–512.....	1998 Jun 10	Mp Hh At Ho, Mk	Nz	Penticton	4.946	14	7
PKS 0438–436.....	1998 Mar 7	Mp Hh At Mk	Tz Rz	Mitaka	4.949	10	5
PKS 0537–441.....	1998 Mar 1	Mp Hh Ho Fd Ov Mk	Gz	Mitaka	4.946	14	3
PKS 0637–752.....	1997 Nov 21	Mp Hh At	Gz Tz	Penticton	4.976	12	6
PKS 0637–752.....	1999 Aug 19	Mp Hh At Ho	Rz Uz	Penticton	4.816	9	8
PKS 1104–445.....	1999 May 27	Mp Hh At Ho So	Rz Uz	Penticton	4.946	7	4
PKS 1127–145.....	1999 Apr 24	Mp VLBA-Mk	Tz Nz	Socorro	4.816	8	4
PKS 1424–418.....	1999 Aug 1	Mp Fd Ov Mk Kp La Pt Sc	Gz	Socorro	4.816	5	3
PKS 1610–771.....	1999 Apr 5	Mp Hh At Ho	Gz Rz Tz	Penticton	4.946	10	8
PKS 1622–253.....	2000 May 22	VLBA	Tz Nz	Socorro	4.816	4	2
PKS 1622–297.....	2000 Apr 25	VLBA	Tz Nz	Socorro	4.816	4	2
PKS 1718–649.....	1999 Mar 25	Hh At Ho	Tz Nz	Penticton	4.946	6	0.25
PKS 2152–699.....	1999 Apr 8	Hh At Ho	Tz Nz Uz	Penticton	4.946	8	2
PKS 2255–282.....	1999 May 18	Mp At Ho VLBA	Rz	Socorro	4.976	2	2
PKS 2355–534.....	1998 Jun 6	Mp Hh	Gz Rz	Penticton	4.946	6	3

NOTE.—Ground telescopes: Mp = Mopra (Australia Telescope National Facility; ATNF); Hh = Hartebeesthoek (Hartebeesthoek Radio Astronomy Observatory; HRAO); At = Australia Telescope Compact Array (ATNF); Ho = Hobart (University of Tasmania); Sh = Sheshan (Shanghai Astronomical Observatory; SAO); Fd = Fort Davis (National Radio Astronomy Observatory; NRAO); Ov = Owens Valley (NRAO); Mk = Mauna Kea (NRAO); Kp = Kitt Peak (NRAO); La = Los Alamos (NRAO); Pt = Pie Town (NRAO); Sc = Saint Croix (NRAO); VLBA = full VLBA (NRAO) Tracking Stations: Nz = Green Bank (NRAO); Rz = Robledo (National Aeronautics and Space Administration; NASA); Gz = Goldstone (NASA); Tz = Tidbinbilla (NASA); Uz = Usuda (ISAS) CORR (Correlator); Penticton = S2 (Dominion Radio Astrophysical Observatory; DRAO); Mitaka = VSOP (National Astronomical Observatory of Japan; NAOJ); and Socorro = VLBA (NRAO).

the VLBA antennas was attached to the (u, v) data at the correlator. For the ground antennas, long experience shows that this a priori amplitude calibration data can usually be considered to be uncertain by less than 20%, and often by less than 10%. This expectation is borne out during imaging. When amplitude self-calibration is possible, the corrections to the amplitudes on the ground antennas are very seldom greater than 20%, more often around the 5%–15% value. The HALCA nominal 5 GHz system temperature of 90 K is stable and with the nominal 5 GHz gain of 0.0062 (Moellenbrock et al. 2000) gives a calibration that appears to be at least as good as the ground antennas; amplitude self-calibration (where possible) yielded corrections seldom greater than 10% for HALCA.

Once the amplitude calibration was applied, all data were fringe-fitted using the task FRING. The two 16 MHz channels were fringe-fitted independently since no calibration was available to remove the instrumental phase and delay offsets between the two channels for data from HALCA. However, all sources except PKS 1718–649 were easily strong enough to be detected in each single 16 MHz channel, on all projected baselines. Thus, in general, no sensitivity or resolution penalty was incurred because of this limitation. For PKS 1718–649, the source was detected only during fringe-fitting on the shortest space baselines or those baselines at a favorable position angle in the (u, v) plane, indicating that the components are heavily resolved on longer baselines, at the sensitivity provided by a single 16 MHz channel. For this source many different fringe-fitting timescales were attempted, and the degree of continuity of the delay and rate solutions were used to confirm that the source was not detected.

If ancillary information was available from the correlator noting the magnitude and sign of the fringe delay for particular antennas, those delays were corrected using the task CLCOR before fringe-fitting, so that smaller delay windows could be used in fringe-fitting. Solution intervals in fringe-fitting varied between 2 and 10 minutes and were chosen to maximize the signal-to-noise ratio of the fitted fringes. A signal-to-noise ratio cutoff of 5–7 was used to ensure the reliability of fringes found by FRING.

The results of fringe-fitting—the fitted delays, rates, and phases—were applied to the data and the visibilities averaged across each 16 MHz channel using the task SPLIT. The two-channel, frequency-averaged data were written to disk as FITS files and then imported into DIFMAP (Shepherd, Pearson, & Taylor 1994) for imaging and (u, v) plane model fitting.

In DIFMAP, the data were vector-averaged into 30 s points and phase self-calibrated to a 1 Jy point-source model that was then discarded. The amplitude and phase data were edited then Fourier-transformed into the image plane using a uniform weighting scheme, cleaned (initially using a tight window around the brightest emission, then slowly extending the windows to include fainter emission), and self-calibrated in phase until the accumulated clean component model matched the visibility amplitudes on the shorter baselines and no obvious residual flux remained to be cleaned. This sometimes entailed switching between uniform weighting and natural weighting, to detect the extended emission of some sources, in order to fit the shortest baselines. Finally, if more than four antennas were present in the data set, amplitude self-calibration over the timescale of the observations was performed. If the array

had a relatively large number of antennas, seven or more, and the data had a high signal-to-noise ratio, then amplitude self-calibration was performed on shorter timescales. For imaging, 512×512 pixel images were used, with 0.05 mas pixel sizes.

Figures 1–8 show the final self-calibrated images for the observations listed in Table 2, along with the corresponding (u, v) coverages. Given the oftentimes sparse and irregular (u, v) coverages resulting from space VLBI observations, errors in the images due to nonuniqueness in the deconvolution step can be significant, as is the case for data from any sparse array. This means that some structures seen in VSOP images cannot be fully trusted; generally low surface brightness extended emission suffers worst from this effect. The effects of deconvolution errors in VSOP data are discussed in detail by Lister et al. (2001a). Since the fainter extended structures in our VSOP images are sometimes difficult to interpret because of these effects, we do not analyze them in detail in this paper. We primarily limit ourselves here to an analysis of the highest brightness temperature features in our images. The study of high brightness temperature emission is one of the main justifications for space VLBI missions, providing information that cannot, in general, be obtained from ground-based VLBI observations.

Figure 9 shows plots of the flux density as a function of distance in the (u, v) plane, for each source. These plots contain comparisons of the final self-calibrated data to the visibilities generated by the final models, showing the fit of the clean components to the data.

After imaging, the (u, v) plane data for each source were model-fitted using the technique outlined by Tingay et al. (2001). For the brightest, most compact component of each source (which in most cases can be identified as the core), the group of clean components representing that component were replaced with a single elliptical Gaussian component with six free parameters. The Gaussian model was fitted to the amplitude and phase data after up-weighting the space visibilities relative to the ground visibilities, in analogy to uniform weighting schemes in imaging (Tingay et al. 2001). The resulting core component model parameters for each source are given in Table 3.

Errors on the parameters of the Gaussian model components were estimated, using the DIFWRAP software (Lovell 2000c), as described in Tingay et al. (2001). In particular, the parameters analyzed were the core flux density and size, the parameters required to estimate the core brightness temperatures, according to the following expression,

$$T_{b,G} = \frac{1.22S}{ab\nu^2},$$

where $T_{b,G}$, S , a , and b are described in Table 3. The frequency of observation is ν (in GHz). The brightness temperatures, estimated from the parameters of the Gaussian models, in the observer's and source comoving frames (corresponding to the source redshift), and the brightness temperature errors, estimated using DIFWRAP (these error estimates also take account of the approximate 10% error in the flux density scale), are also given in Table 3. For components with estimated lower limits on the component sizes (upper limits on the brightness temperature) from the above analysis, these estimates are consistent with theoretical estimates of the smallest possible measurable sizes, given a par-

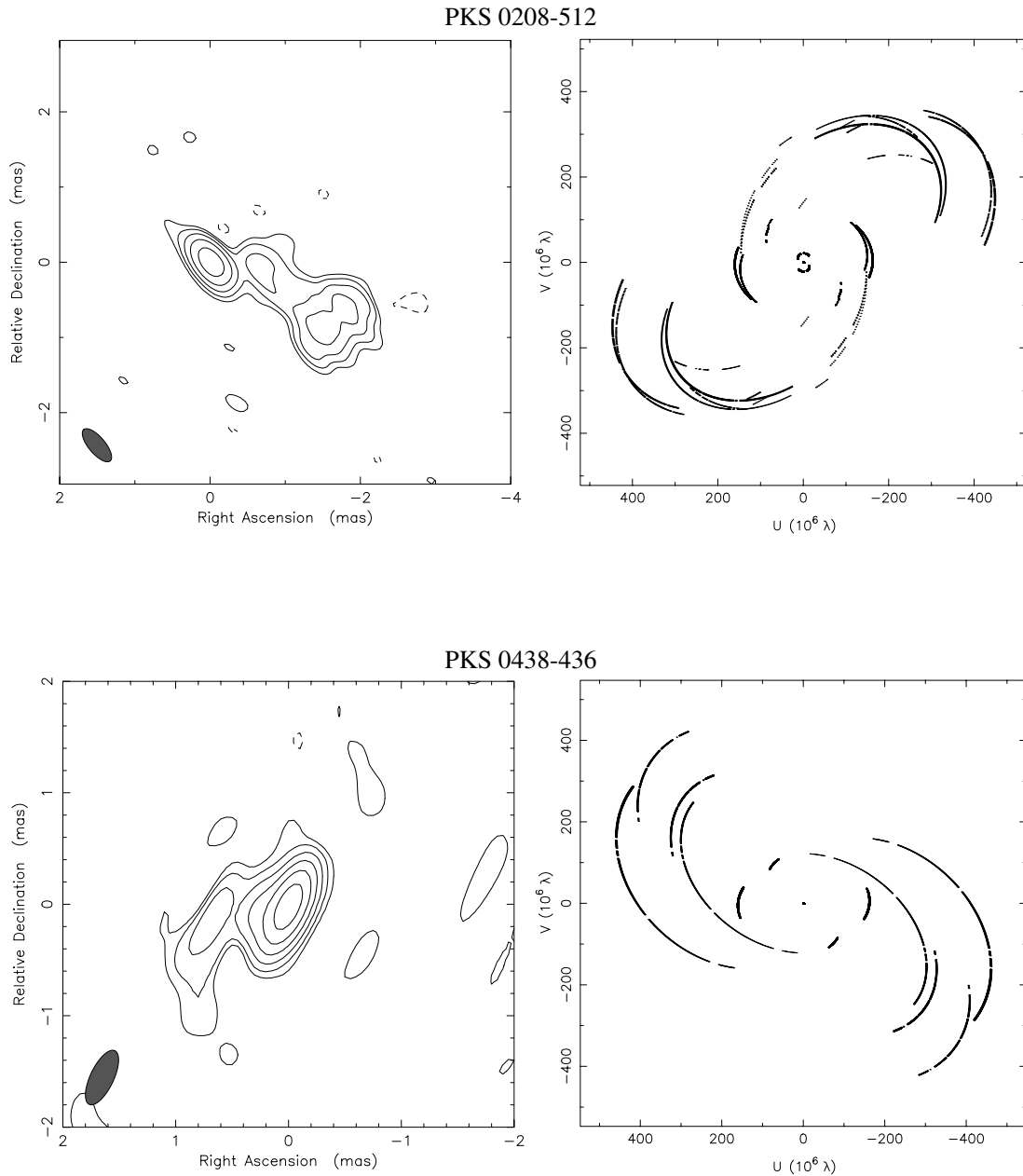


FIG. 1.—*Top*: PKS 0208–512 observed on 1998 June 10 at 4.946 GHz, image (*left*) and (u, v) coverage (*right*). The peak flux density is $0.55 \text{ Jy beam}^{-1}$; contours are -4% , 4% , 8% , 16% , 32% , and 64% of peak; and beam size is $0.55 \times 0.22 \text{ mas}$ at P.A. $40^\circ 2$. *Bottom*: PKS 0438–436 observed on 1998 March 7 at 4.946 GHz, image (*left*) and (u, v) coverage (*right*). The peak flux density is $1.02 \text{ Jy beam}^{-1}$; contours are -2% , 2% , 4% , 8% , 16% , 32% , and 64% of peak; and beam size is $0.53 \times 0.21 \text{ mas}$ at P.A. $-25^\circ 1$.

ticular integrated signal-to-noise ratio, maximum baseline length, and integrated flux density, as calculated by Lovell et al. (2000a).

Table 3 shows that half ($\frac{7}{14}$) of the brightness temperature estimates for the core components admit only a lower limit ($\frac{7}{12}$ of the quasars). This is because during the error analysis the visibility data were often found to be consistent with a core component of zero extent in at least one dimension, either a point-source component or a one-dimensional Gaussian. In either case, the solid angle subtended by the core component is zero, formally giving an infinite brightness temperature. In all cases lower limits to the core brightness temperatures were found, indicating that the

VSOP data constrain the upper limit to the size of the core component very well. Sensitivity to the brightness temperature lower limit and insensitivity to the upper limit for core components is commonplace when dealing with VSOP data, as evidenced by the similar results obtained from a VSOP study of the Pearson-Readhead VLBI sample (Tingay et al. 2001; Lister et al. 2001a; Lister, Tingay, & Preston 2001b) and the VSOP Survey of compact extragalactic radio sources (Hirabayashi et al. 2000b).

Figure 10 shows the brightness temperature estimates in the observer's frame and in the source frame, with errors, for the sources listed in Table 3. Gamma-ray sources are those identified by the EGRET instrument at energies above

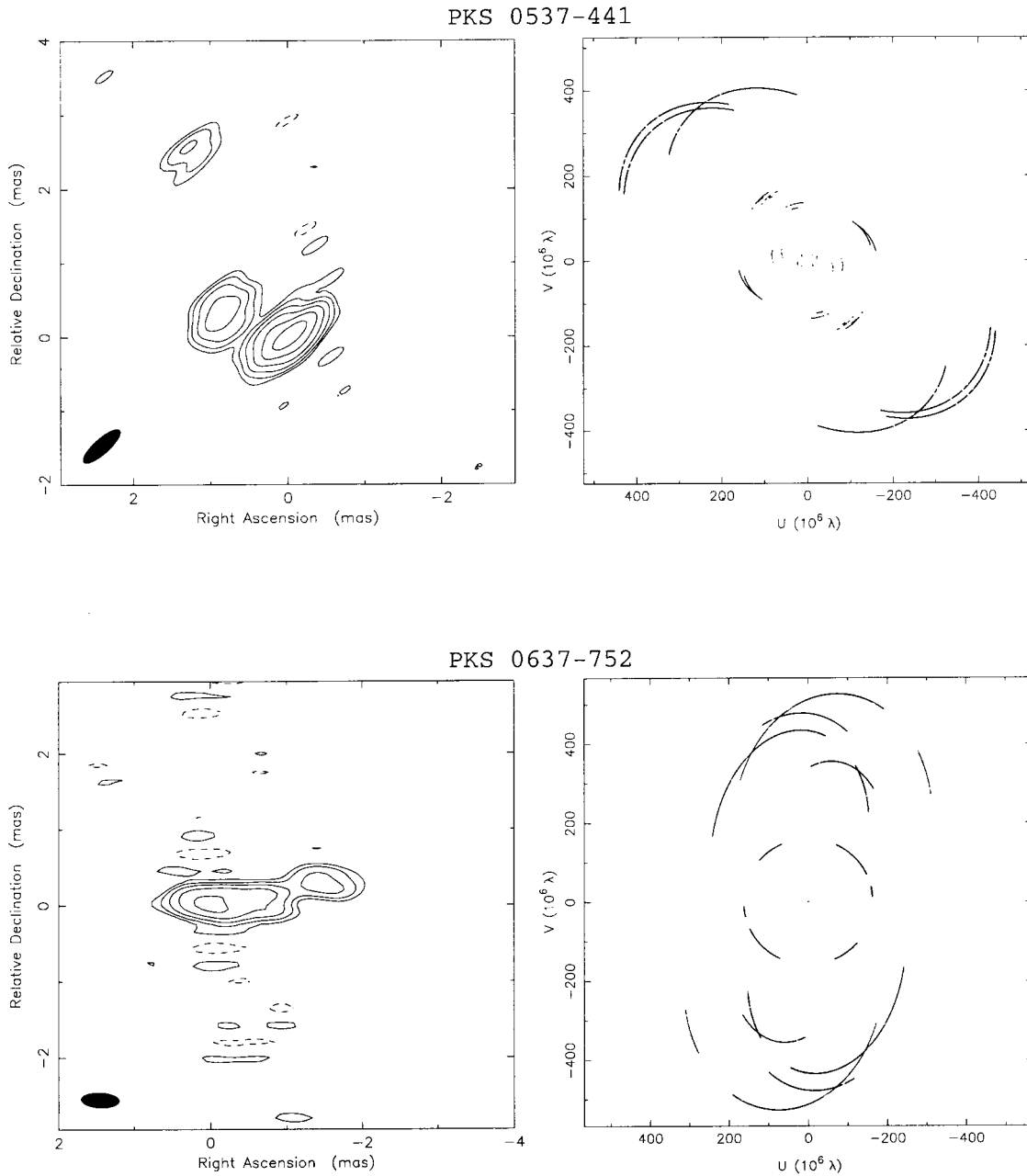


FIG. 2.—*Top:* PKS 0537-441 observed on 1998 March 1 at 4.946 GHz, image (*left*) and (u, v) coverage (*right*). The peak flux density is $0.50 \text{ Jy beam}^{-1}$; contours are -2% , 2% , 4% , 8% , 16% , 32% , and 64% of peak; and beam size is $0.63 \times 0.20 \text{ mas}$ at P.A. $-47^\circ 3$. *Bottom:* PKS 0637-752 observed on 1997 November 21 at 4.976 GHz, image (*left*) and (u, v) coverage (*right*). The peak flux density is $0.73 \text{ Jy beam}^{-1}$; contours are -5% , 5% , 10% , 20% , 40% , and 80% of peak; and beam size is $0.50 \times 0.19 \text{ mas}$ at P.A. $87^\circ 2$.

100 MeV, as listed in the third EGRET catalog (Hartman et al. 1999). A comparison of the brightness temperature distributions of the gamma-ray-loud and gamma-ray-quiet sources is discussed in § 4.

2.2. Geodetic VLBI Data

We have extracted geodetic VLBI data from the United States Naval Observatory (USNO) database for three of the sources from Table 1, PKS 0208-512, PKS 0537-441, and PKS 1610-771. Data for a fourth source, PKS 0637-752, have been described elsewhere (Schwartz et al. 2000; Lovell et al. 2000b). The USNO database is used primarily for geodetic work, but the VLBI data also contain useful astro-

nomical information on source structure, although the data quality for astronomical applications is below that produced by VLBI arrays dedicated to astronomical measurements, and the dynamic ranges and sensitivities of the corresponding images are lower. Examples of astronomical results from the USNO geodetic database appear in Tateyama et al. (1999) and Piner & Kingham (1998).

Table 4 lists the geodetic VLBI observations extracted from the archive at the USNO correlator in Washington DC. For each observation, data have been obtained simultaneously at 2.3 and 8.4 GHz. Since each individual geodetic experiment contains only a relatively small amount of data, we have combined data from experiments over periods of

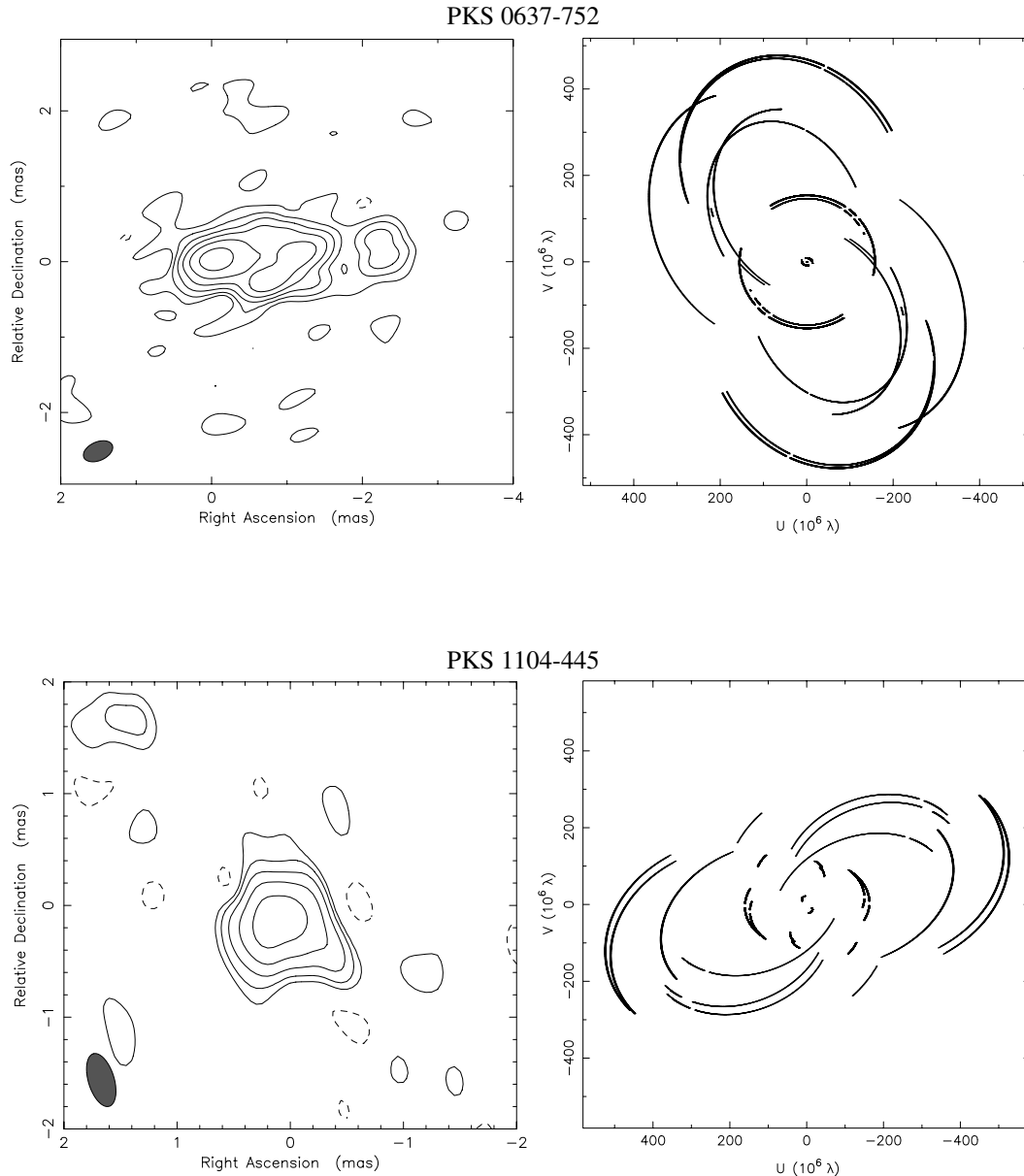


FIG. 3.—*Top*: PKS 0637–752 observed on 1999 August 19 at 4.816 GHz, image (*left*) and (u, v) coverage (*right*). The peak flux density is $0.87 \text{ Jy beam}^{-1}$; contours are -2% , 2% , 4% , 8% , 16% , 32% , and 64% of peak; and beam size is $0.41 \times 0.25 \text{ mas}$ at P.A. $-66^\circ 5$. *Bottom*: PKS 1104–445 observed on 1999 May 27 at 4.946 GHz, image (*left*) and (u, v) coverage (*right*). The peak flux density is $0.41 \text{ Jy beam}^{-1}$; contours are -4% , 4% , 8% , 16% , 32% , and 64% of peak; and beam size is $0.49 \times 0.23 \text{ mas}$ at P.A. $16^\circ 5$.

time ranging up to 20 days, to produce imagable data sets. Table 4 indicates the time ranges over which different data sets have been combined to produce single imagable data sets. These data have been fringe-fitted and calibrated as described in Piner & Kingham (1998) using AIPS, with imaging and model fitting undertaken in DIFMAP. For imaging, 128×128 pixel maps have been used with 0.5 mas pixels for the 2.3 GHz data and 0.1 mas pixels for the 8.4 GHz data. Uniform weighting has been used for all images with phase self-calibration but no amplitude self-calibration. Circular Gaussian model components have generally been used in model fitting. The models have been fitted to

the self-calibrated data subsequent to the imaging process, with further self-calibration to ensure the best fit to the data. A typical (u, v) coverage is shown in Figure 11.

At 2.3 GHz the beam sizes for the observations listed in Table 4 are typically between 1.5 and 2.5 mas and the rms noise level in the resulting images ranges between 10 and 50 mJy beam^{-1} . At 8.4 GHz, the beam sizes are typically between 0.4 and 0.6 mas, and the rms noise level in the images also ranges between 10 and 50 mJy beam^{-1} .

The geodetic VLBI images can be seen in Figures 12, 13, and 14. Figure 12 shows the series of five images of PKS 0208–512 at 2.3 and 8.4 GHz. Figure 13 shows the series of

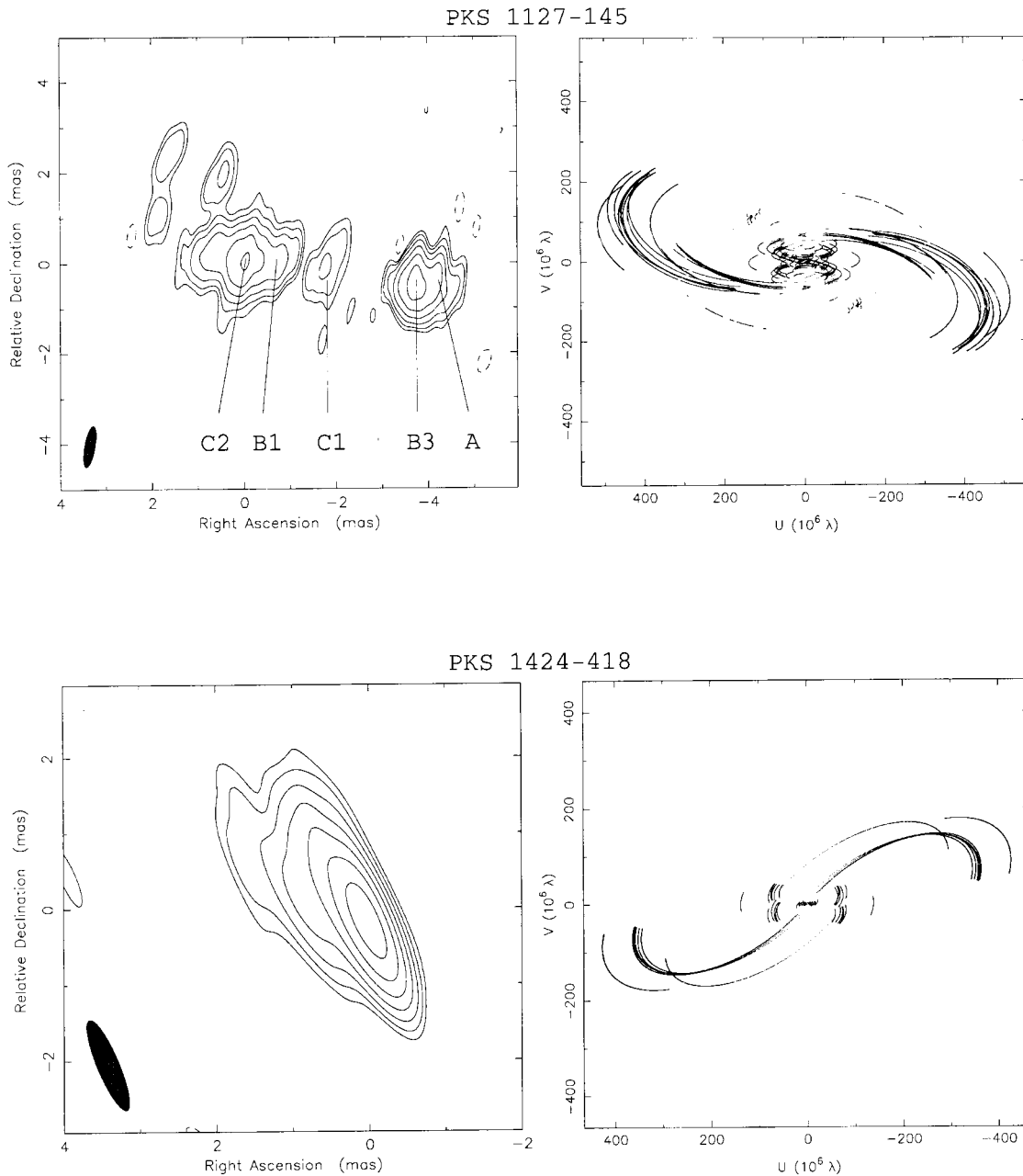


FIG. 4.—*Top:* PKS 1127–145 observed on 1999 April 24 at 4.816 GHz, image (*left*) and (u, v) coverage (*right*). The peak flux density is $0.42 \text{ Jy beam}^{-1}$; contours are -2% , 2% , 4% , 8% , 16% , 32% , and 64% of peak; and beam size is $0.92 \times 0.23 \text{ mas}$ at P.A. $-10^\circ 2$. *Bottom:* PKS 1424–418 observed on 1999 August 01 at 4.816 GHz, image (*left*) and (u, v) coverage (*right*). The peak flux density is $0.88 \text{ Jy beam}^{-1}$; contours are -1% , 1% , 2% , 4% , 8% , 16% , 32% , and 64% of peak; and the beam size is $1.29 \times 0.29 \text{ mas}$ at P.A. $22^\circ 4$.

four images of PKS 0537–441 at 2.3 and 8.4 GHz. Figure 14 shows the series of seven images of PKS 1610–771 at 2.3 and 8.4 GHz.

The PKS 0208–512 2.3 GHz geodetic data can be model-fitted at each epoch with a dual-component model, representing a core and an extended jet component along a position angle of approximately -130° (Table 5). Figure 15 shows the separation between the core and jet components as a function of time. For comparison, also shown are the component separations from the 4.8 GHz observation of Tingay et al. (1996a) of 1992 November and the 4.9 GHz VSOP space VLBI observation of 1998 June (Fig. 1). The component separation from the VSOP data has been measured from the image in DIFMAP, and an error of one

beamwidth has been adopted, in recognition of the likely errors due to the (u, v) coverage. The separation between the core and jet components from the 1992 November observation is consistent with the new results at 2.3 GHz from the geodetic archive data. There is no evidence for an increase in the separation between the core and jet components between 1992 November and 1998 June. A weighted linear least-squares fit to the data give the apparent separation speed to be $0.07 \pm 0.09 \text{ mas yr}^{-1}$, corresponding to $\beta_{\text{app}} = (2.4 \pm 3.1) h^{-1}$, where β_{app} is the apparent transverse speed of separation, in units of the speed of light and the Hubble constant is $H_0 = 100 h$.

At 8.4 GHz, the PKS 0208–512 data at only two of the five epochs required a two-component model, representing

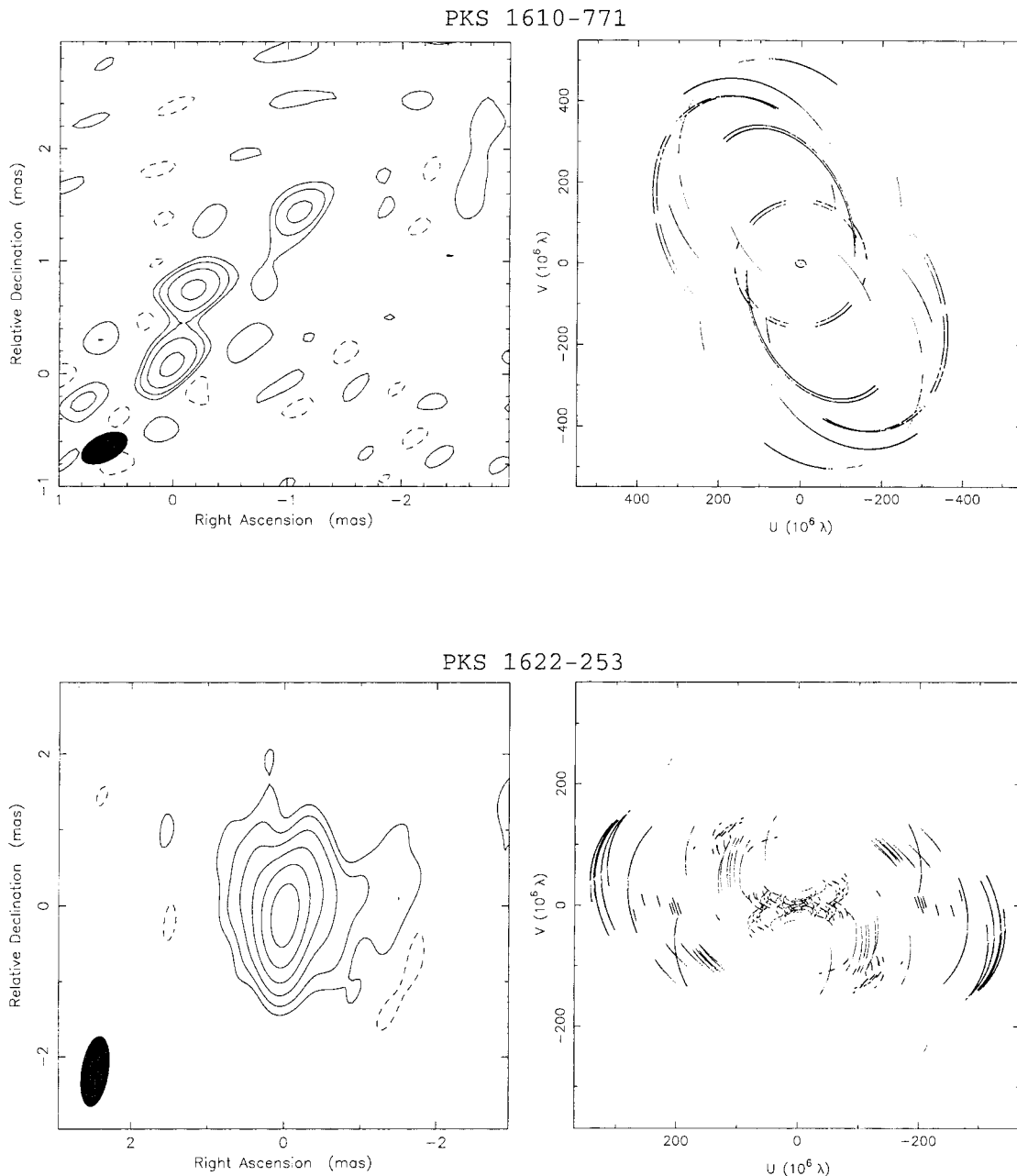


FIG. 5.—*Top*: PKS 1610–771 observed on 1999 April 05 at 4.946 GHz, image (*left*) and (u, v) coverage (*right*). The peak flux density is $0.15 \text{ Jy beam}^{-1}$; contours are -10% , 10% , 20% , 40% , and 80% of peak; and beam size is $0.44 \times 0.23 \text{ mas}$ at P.A. $-63^\circ 3'$; *Bottom*: PKS 1622–253 observed on 2000 May 22 at 4.816 GHz, image (*left*) and (u, v) coverage (*right*). The peak flux density is $0.37 \text{ Jy beam}^{-1}$; contours are -2% , 2% , 4% , 8% , 16% , 32% , and 64% of peak; and beam size is $0.93 \times 0.35 \text{ mas}$ at P.A. $-8^\circ 7'$.

core and jet (Table 5). At three epochs only a single-component model was required to fit the data, representing only the core (Table 5). We suggest that this is because at the higher frequency the extended jet component may be more difficult to detect with the limited data, owing to resolution and spectral index effects. At the two epochs where two-component models were used, the separation and position angle between the components were consistent, within the uncertainties, with the 2.3 GHz model fits.

PKS 0537–441 at 8.4 GHz is resolved into a core and jet component with approximately 0.4 mas separation at a position angle of approximately 90° and has been model-fitted as such (Table 6). The only VLBI images of PKS 0537–441 previously published (Tingay et al. 1996a) show

an extension to the core toward the north, offset 90° from the extension to the core we see in the current data. The 4.9 GHz observation of PKS 0537–441 made with the VSOP data (Fig. 2) clarifies the situation; it shows that the jet initially emerges from the core at a position angle close to 90° and undergoes an apparent bend toward the north. The extension close to the core is apparent only in the highest resolution images, the VSOP and geodetic images. The extension to the north is weak and detected only in the high-sensitivity images, the images of Tingay et al. (1996a), and the VSOP image.

The 8.4 GHz images of PKS 0537–441 give valuable confirmation that the high-resolution structure shown in the VSOP image is correct. Figure 15 shows the separa-

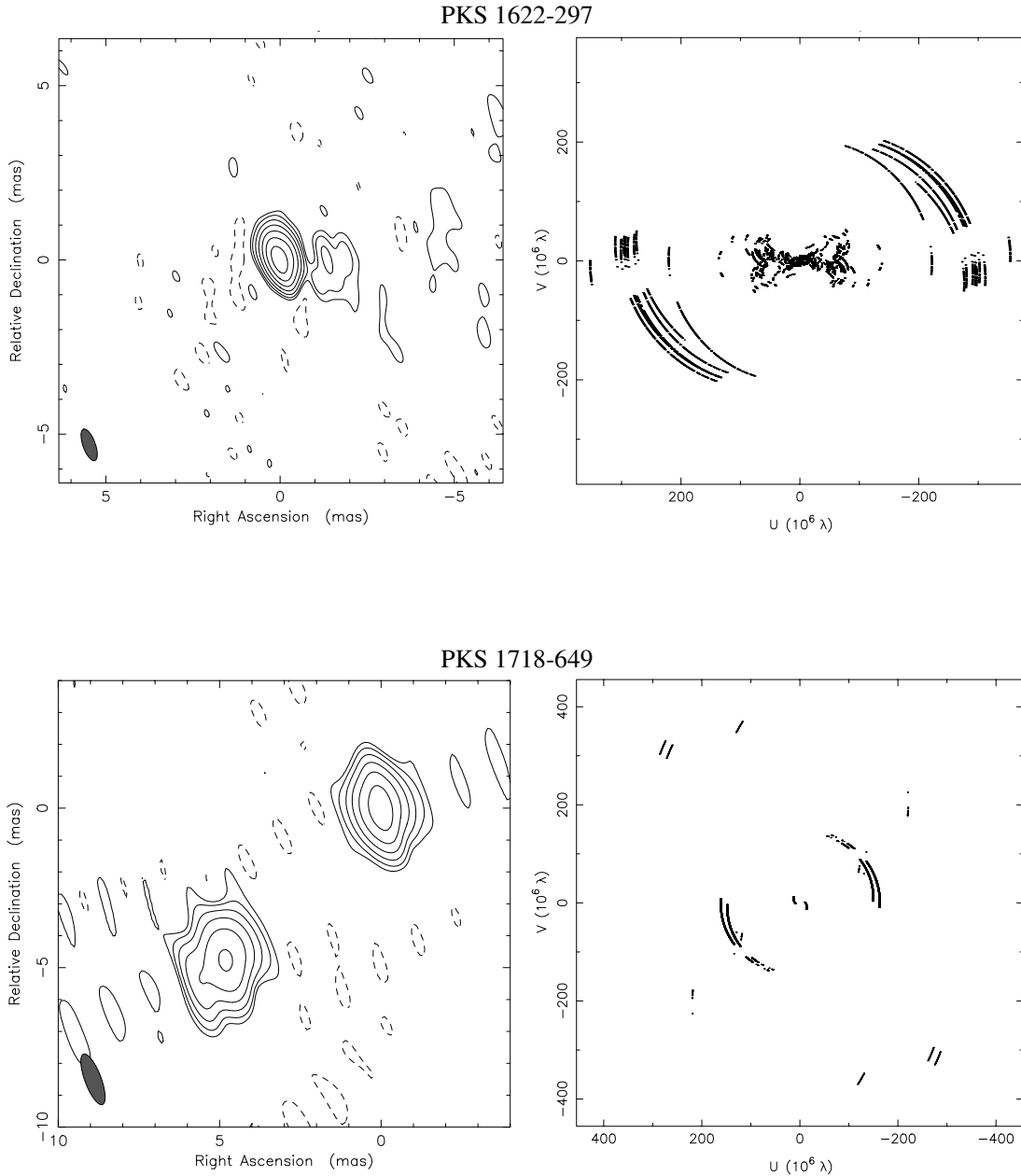


FIG. 6.—*Top*: PKS 1622–297 observed on 2000 April 25 at 4.816 GHz, image (*left*) and (u, v) coverage (*right*). The peak flux density is $0.93 \text{ Jy beam}^{-1}$; contours are -1% , 1% , 2% , 4% , 8% , 16% , 32% , 64% of peak; and beam size is $0.96 \times 0.35 \text{ mas}$ at P.A. 20° . *Bottom*: PKS 1718–649 observed on 1999 March 25 at 4.946 GHz, image (*left*) and (u, v) coverage (*right*). The peak flux density is $0.62 \text{ Jy beam}^{-1}$; contours are -2% , 2% , 4% , 8% , 16% , 32% , and 64% of peak; and beam size is $1.69 \times 0.51 \text{ mas}$ at P.A. $20^\circ.3$.

tion of the jet component from the core as a function of time. Also shown is the separation as measured from the VSOP image at 4.9 GHz, from 1998 March. As for PKS 0208–512, the separation from the VSOP data was measured from the image in DIFMAP and one beamwidth is adopted as the error. No evidence for a change in separation over the course of the geodetic observations is apparent. However, comparing the geodetic data to the VSOP data may allow a better estimate of the component proper motion. A weighted linear least-squares fit to the separation as a function of time gives an apparent speed of $0.09 \pm 0.07 \text{ mas yr}^{-1}$, corresponding to $\beta_{\text{app}} = (2.8 \pm 2.2) h^{-1}$, only a very tentative detection of motion, especially given that the separation change is

entirely due to the VSOP data, at a different frequency and resolution from the geodetic data.

At 2.3 GHz the resolution of the PKS 0537–441 images is not high enough to resolve the core and jet components, and the sensitivity of the observations is not high enough to detect the northern component. Each 2.3 GHz data set can be adequately model-fitted with a single circular Gaussian component (Table 6).

PKS 1610–771 is resolved at both 2.3 and 8.4 GHz. At 2.3 GHz, this source consists of a bright unresolved source and an extension along a position angle of approximately -40° ; 2.3 GHz model fits are given in Table 7 (we have relaxed the requirement that only circular Gaussian components be used in the 2.3 GHz model fits for PKS 1610–771,

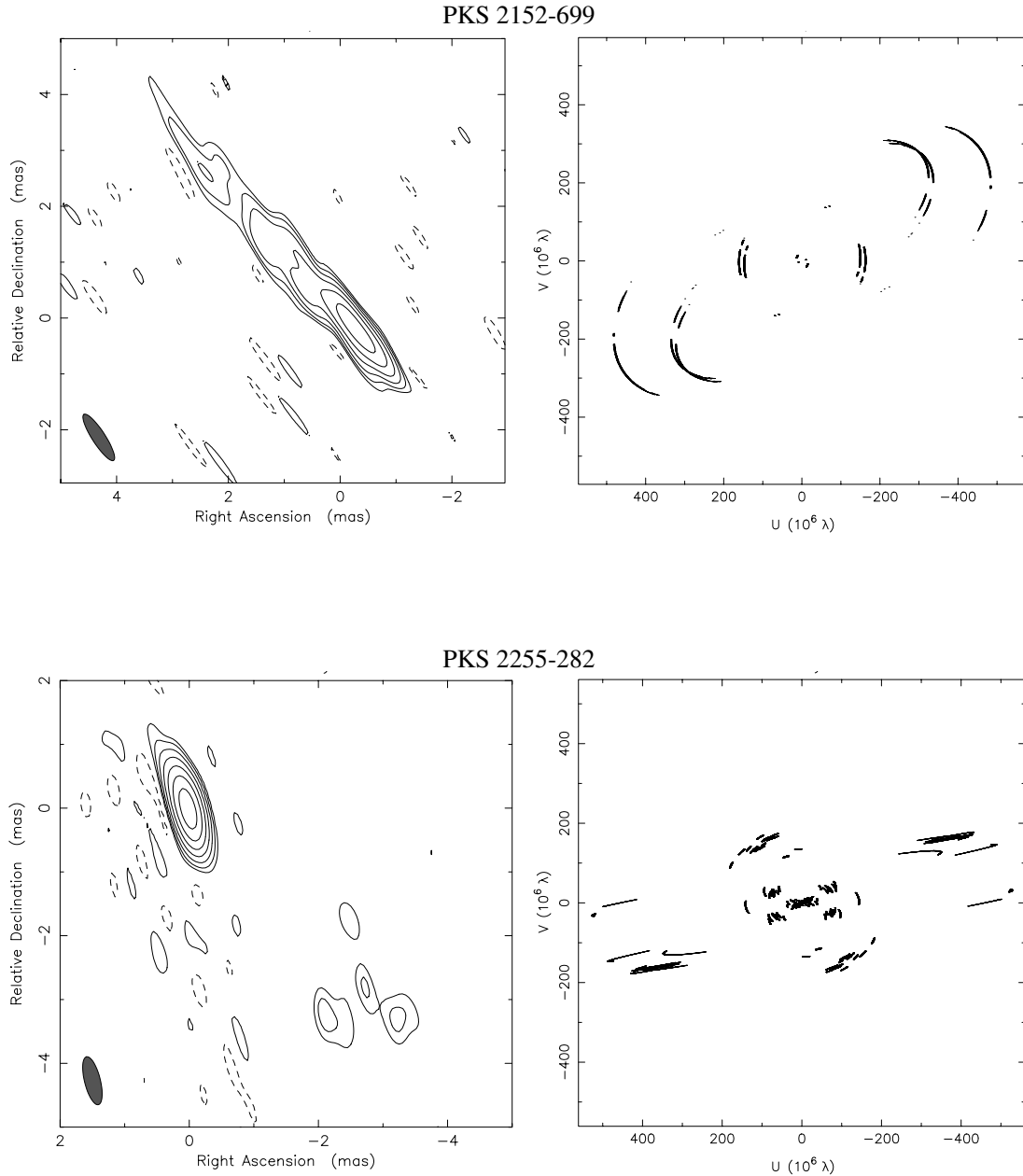


FIG. 7.—*Top*: PKS 2152–699 observed on 1999 April 08 at 4.946 GHz, image (*left*) and (u, v) coverage (*right*). The peak flux density is $0.13 \text{ Jy beam}^{-1}$; contours are -2% , 2% , 4% , 8% , 16% , 32% , and 64% of peak; and beam size is $0.98 \times 0.23 \text{ mas}$ at P.A. $32^\circ 9'$. *Bottom*: PKS 2255–282 observed on 1999 May 18 at 4.976 GHz, image (*left*) and (u, v) coverage (*right*). The peak flux density is $2.13 \text{ Jy beam}^{-1}$; contours are -1% , 1% , 2% , 4% , 8% , 16% , 32% , and 64% of peak; and beam size is $0.77 \times 0.25 \text{ mas}$ at P.A. $13^\circ 8'$.

in order to efficiently model the extended structure). No consistent evolution of the source structure can be seen at 2.3 GHz.

At 8.4 GHz, PKS 1610–771 is resolved into two compact components that can clearly be seen to separate, on inspection of Figure 14, also confirming the structural position angle seen at 2.3 GHz. It should be noted that at 1993.44, the flux densities of these two compact components appear to be reversed, probably owing to a π phase ambiguity due to a low signal-to-noise ratio and sparse (u, v) coverage. The model fits of the 8.4 GHz data show that at each epoch (except for the first, 1993.09), the best fit is achieved by a two-component model (Table 7). The separation of these

two components as a function of time is shown in Figure 15. A weighted linear least-squares fit to these separations gives a proper motion of $0.19 \pm 0.07 \text{ mas yr}^{-1}$, corresponding to an apparent transverse speed of $\beta_{\text{app}} = (9.4 \pm 3.5) h^{-1}$.

These dual-frequency geodetic images of PKS 1610–771 could be interpreted as follows. The weak component at 8.4 GHz is actually the stationary core of the source, and the strong component (fixed at the phase center in the 8.4 GHz images) is the component in motion, toward the northwest. Both components in the 8.4 GHz images contribute to the extended component at the phase center of the 2.3 GHz images, with further extended jet emission detected to the northwest.

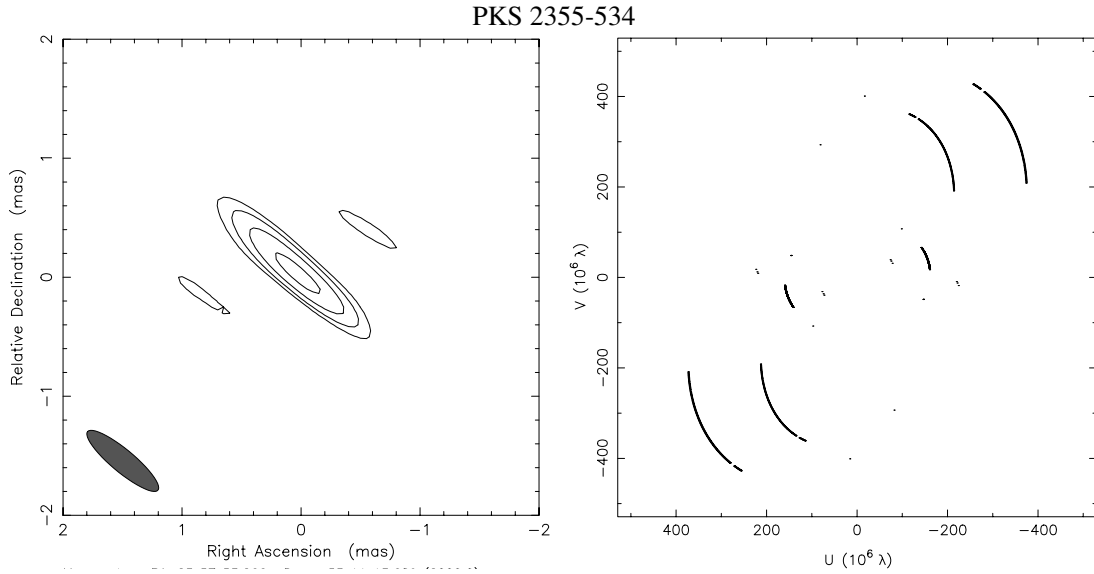


FIG. 8.—PKS 2355–534 observed on 1998 June 06 at 4.946 GHz, image (*left*) and (u, v) coverage (*right*). The peak flux density is $0.31 \text{ Jy beam}^{-1}$; contours are -10% , 10% , 20% , 40% , and 80% of peak; and beam size is $0.77 \times 0.19 \text{ mas}$ at P.A. $50^\circ 2$.

3. NOTES ON INDIVIDUAL SOURCES

3.1. PKS 0208–512

Ground-based VLBI images of this source at 5 GHz are reported by Tingay et al. (1996a) and Shen et al. (1998). Both images show a bright core and a marginally resolved extension along a position angle of 233° (angular resolution of approximately 2 mas in both cases). The VSOP image (Fig. 1) resolves this source into a clear core-jet structure, in agreement with the lower resolution ground-based images (including the geodetic images from § 2.2); close to the core the jet emerges at a position angle of approximately 270° ,

then bends to the south. At the end of the jet an extended component (or blend of components) appears to lie perpendicular to the jet direction. The orientation of this component relative to the jet direction is strongly indicated in the closure phase information from triangles involving HALCA, indicating that this structure is not an artifact of the (u, v) coverage.

3.2. PKS 0438–436

VLBI images at 2.3 GHz by Preston et al. (1989; 14 mas resolution) and Murphy et al. (1993; no angular resolution

TABLE 3
GAUSSIAN BEST-FIT MODELS FOR THE BRIGHTEST, MOST COMPACT COMPONENT IN EACH IMAGE

Source (1)	S (2)	R (3)	θ (deg) (4)	a (5)	b/a (6)	ϕ (deg) (7)	$T_{b,G}$ (8)	$T_{b-co,G}$ (9)	ν_{co} (10)
PKS 0208–512.....	0.6 ± 0.2	0.0	0	$0.4 \pm \begin{smallmatrix} 0.2 \\ 0.3 \end{smallmatrix}$	<0.6	50	$0.4 \pm \begin{smallmatrix} \text{inf} \\ 0.3 \end{smallmatrix}$	$0.8 \pm \begin{smallmatrix} \text{inf} \\ 0.6 \end{smallmatrix}$	9.9
PKS 0438–436.....	1.0 ± 0.2	0.0	0	$0.3 \pm \begin{smallmatrix} 0.1 \\ 0.0 \end{smallmatrix}$	$0.5 \pm \begin{smallmatrix} 0.1 \\ 0.2 \end{smallmatrix}$	-42	$1.1 \pm \begin{smallmatrix} 0.1 \\ 0.7 \end{smallmatrix}$	$4.3 \pm \begin{smallmatrix} 0.4 \\ 2.3 \end{smallmatrix}$	19.0
PKS 0537–441.....	$0.8 \pm \begin{smallmatrix} 0.2 \\ 0.3 \end{smallmatrix}$	0.0	0	0.3 ± 0.1	$0.8 \pm \begin{smallmatrix} 0.2 \\ 0.3 \end{smallmatrix}$	-67	$0.6 \pm \begin{smallmatrix} 2.0 \\ 0.3 \end{smallmatrix}$	$1.0 \pm \begin{smallmatrix} 0.7 \\ 3.8 \end{smallmatrix}$	9.4
PKS 0637–752.....	$1.3 \pm \begin{smallmatrix} 0.6 \\ 0.2 \end{smallmatrix}$	0.0	0	$0.6 \pm \begin{smallmatrix} 0.3 \\ 0.1 \end{smallmatrix}$	0.3 ± 0.1	73	$0.6 \pm \begin{smallmatrix} 1.5 \\ 0.4 \end{smallmatrix}$	$1.0 \pm \begin{smallmatrix} 2.4 \\ 0.7 \end{smallmatrix}$	8.2
PKS 1104–445.....	0.4 ± 0.1	0.0	0	$0.3 \pm \begin{smallmatrix} 0.3 \\ 0.1 \end{smallmatrix}$	<1.0	-27	$0.6 \pm \begin{smallmatrix} \text{inf} \\ 0.4 \end{smallmatrix}$	$1.4 \pm \begin{smallmatrix} \text{inf} \\ 1.0 \end{smallmatrix}$	12.8
PKS 1127–145.....	0.4 ± 0.1	4.3	-97	$0.2 \pm \begin{smallmatrix} 0.0 \\ 0.1 \end{smallmatrix}$	<0.6	0	>0.6	>1.3	10.5
PKS 1424–418.....	0.9 ± 0.2	0.0	0	$0.2 \pm \begin{smallmatrix} 0.4 \\ 0.0 \end{smallmatrix}$	<1.0	-10	$1.2 \pm \begin{smallmatrix} \text{inf} \\ 0.8 \end{smallmatrix}$	$3.1 \pm \begin{smallmatrix} \text{inf} \\ 2.1 \end{smallmatrix}$	12.1
PKS 1610–771.....	$0.9 \pm \begin{smallmatrix} 0.2 \\ 0.5 \end{smallmatrix}$	0.0	0	$0.8 \pm \begin{smallmatrix} 0.4 \\ 0.5 \end{smallmatrix}$	<0.8	-33	$0.2 \pm \begin{smallmatrix} \text{inf} \\ 0.1 \end{smallmatrix}$	$0.6 \pm \begin{smallmatrix} \text{inf} \\ 0.5 \end{smallmatrix}$	13.0
PKS 1622–253.....	0.6 ± 0.2	0.0	0	<1.0	<1.0	-6	$0.2 \pm \begin{smallmatrix} \text{inf} \\ 0.1 \end{smallmatrix}$	$0.3 \pm \begin{smallmatrix} \text{inf} \\ 0.1 \end{smallmatrix}$	8.8
PKS 1622–297.....	1.5 ± 0.3	0.0	0	0.4 ± 0.1	$0.8 \pm \begin{smallmatrix} 0.2 \\ 0.7 \end{smallmatrix}$	-65	$0.6 \pm \begin{smallmatrix} 5.1 \\ 0.4 \end{smallmatrix}$	$1.1 \pm \begin{smallmatrix} 9.5 \\ 0.5 \end{smallmatrix}$	8.7
PKS 1718–649.....	$1.3 \pm \begin{smallmatrix} 0.2 \\ 0.3 \end{smallmatrix}$	0.0	0	1.0 ± 0.4	0.4 ± 0.2	-62	$0.1 \pm \begin{smallmatrix} 0.9 \\ 0.05 \end{smallmatrix}$	$0.1 \pm \begin{smallmatrix} 0.9 \\ 0.05 \end{smallmatrix}$	5.0
	1.1 ± 0.3	6.7	134	1.3 ± 0.5	0.4 ± 0.2	-49	$0.1 \pm \begin{smallmatrix} 0.7 \\ 0.07 \end{smallmatrix}$	$0.1 \pm \begin{smallmatrix} 0.7 \\ 0.07 \end{smallmatrix}$	5.0
PKS 2152–699.....	0.3 ± 0.1	0.3	-130	0.9 ± 0.2	0.2 ± 0.1	42	$0.1 \pm \begin{smallmatrix} 0.3 \\ 0.05 \end{smallmatrix}$	$0.1 \pm \begin{smallmatrix} 0.3 \\ 0.05 \end{smallmatrix}$	5.1
PKS 2255–282.....	2.7 ± 0.4	0.0	0	0.3 ± 0.1	$0.4 \pm \begin{smallmatrix} 0.4 \\ 0.2 \end{smallmatrix}$	27	$3.6 \pm \begin{smallmatrix} 15.2 \\ 2.6 \end{smallmatrix}$	$7.0 \pm \begin{smallmatrix} 29.5 \\ 5.2 \end{smallmatrix}$	9.6
PKS 2355–534.....	$0.4 \pm \begin{smallmatrix} 0.2 \\ 0.1 \end{smallmatrix}$	0.0	0	<0.3	<0.5	49	>0.4	>0.8	9.9

NOTE.—Col. (1): source; col. (2): S , the integrated flux density of the model component in Jy; col. (3): R , the distance of the model component from the designated phase center in milliarcseconds; col. (4): θ , the position angle of the model component centroid from the designated phase center in degrees east of north; col. (5): a , the major-axis extent (FWHM) of the model component in milliarcseconds; col. (6): b/a , the ratio of model component minor axis to major-axis extent; col. (7): ϕ , the position angle of the model component major axis in degrees east of north; col. (8): $T_{b,G}$, the observed brightness temperature of the Gaussian component, in units of 10^{12} K ; col. (9): $T_{b-co,G}$, the source-frame (comoving) brightness temperature of the Gaussian component, in units of 10^{12} K ; and col. (10): ν_{co} , the frequency of the observed emission in the source frame in GHz.

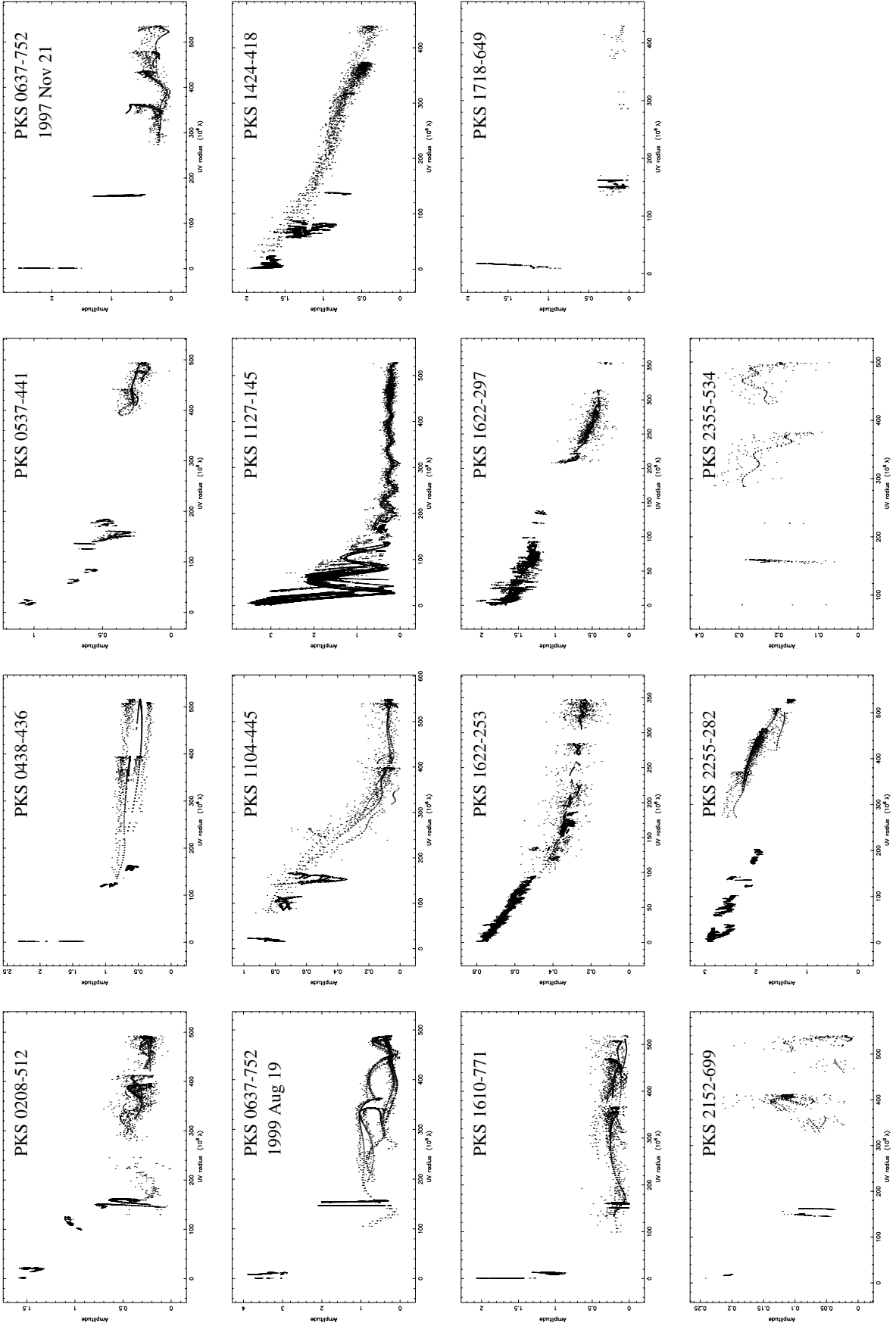


FIG. 9.—Flux density vs. (u, v) distance for each of the sources—self-calibrated data and final model

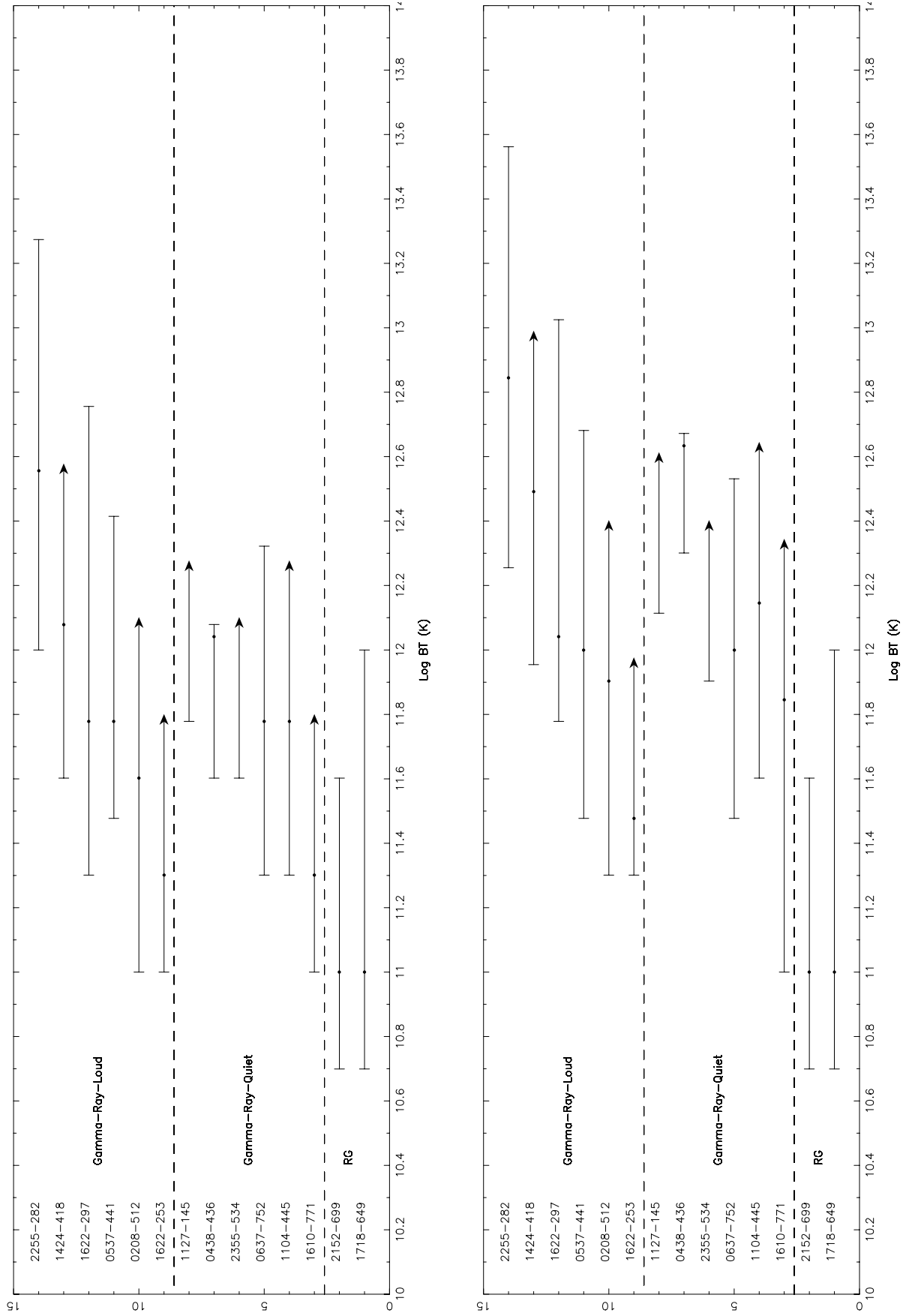


FIG. 10.—*Top*: Observer-frame Gaussian component brightness temperature estimates for the 14 sources observed with VSOP. *Bottom*: Source-frame Gaussian component brightness temperature estimates (i.e., corrected for redshift). In both plots, RG denotes radio galaxy.

TABLE 4
LOG OF GEODETIC VLBI OBSERVATIONS

Source	Mean Date	Date Range (days)	Antennas
PKS 0208–512.....	1993.11	1	O, Hb, S, E, Dt
PKS 0208–512.....	1993.73	20	O, Hb, S, E, F
PKS 0208–512.....	1994.13	5	O, Hb, S, E, Dt
PKS 0208–512.....	1994.73	6	Hb, S, E, Ft, F, K
PKS 0208–512.....	1995.16	5	O, Hb, S, E, Dt, F
PKS 0537–441.....	1993.08	10	O, Hb, S, E, Dt
PKS 0537–441.....	1995.24	16	O, Hb, S, Dt, F, K, Ka
PKS 0537–441.....	1995.53	1	Hb, S, E, Dt, F
PKS 0537–441.....	1995.75	11	O, Hb, S, E, Dt, F, K, Dg
PKS 1610–771.....	1993.09	5	O, Hb, S, E, Dt
PKS 1610–771.....	1993.44	1	Hb, S, E, Dt
PKS 1610–771.....	1993.91	5	Hb, E, Dt, F
PKS 1610–771.....	1994.12	1	O, Hb, S, E, Dt
PKS 1610–771.....	1995.12	10	O, Hb, S, E, Dt, F
PKS 1610–771.....	1995.58	7	Hb, S, E, Dt, F
PKS 1610–771.....	1995.84	7	O, Hb, S, E, Dt, F

NOTE.—Antenna designations: O = O’Higgins; Hb = Hobart; S = Santiago; E = Hartebeesthoek; Dt = DSN, Tidbinbilla; F = Fortleza; K = Kokee; Ka = Kashima; and Dg = DSN, Goldstone.

quoted) show that PKS 0438–436 consists of two components separated by approximately 35 mas along a position angle of -43° . Tingay et al. (1998b) presents a higher resolution (3 mas) VLBI image at 4.8 GHz that resolves the structure of these two components and shows that both are elongated, but neither along the position angle that joins them. A slightly higher resolution (2 mas) ground-based image at 4.8 GHz by Shen et al. (1998) shows that the southern component is heavily resolved, whereas the northern component (presumably the core) remains compact. The VSOP image (Fig. 1) detects only the northern component,

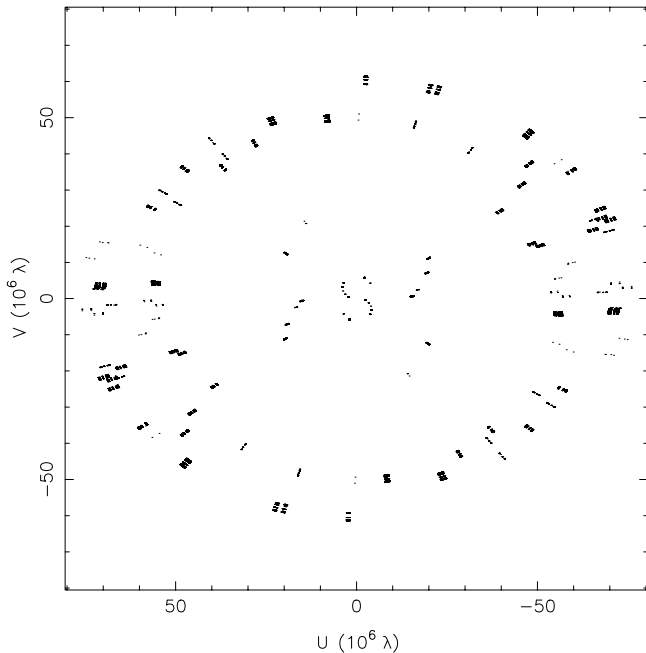


FIG. 11.—Sample (u, v) coverage for a geodetic VLBI observation of PKS 0208–512 at 2.3 GHz, from 1994.13.

and the southern component is fully resolved on the baselines to HALCA; it shows a compact core and an extension to the east approximately 1 mas in length, in the direction of the extension seen from previous ground-based observations.

3.3. PKS 0537–441

PKS 0537–441 has previously been imaged by Tingay et al. (1996a; 4.8 and 8.4 GHz, 7 and 2 mas resolution, respectively) and Shen et al. (1998; 4.8 GHz, 3 mas resolution). All three images show an approximately 4 mas northern extension to a bright, compact core. The value of the VSOP resolution is again apparent in the new image (Fig. 2). The extension to the core is now resolved into a jet that curves over its 4 mas length. Close to the core the jet has a position angle of approximately 60° , the jet then curves to the north, in agreement with the lower resolution ground-based images. This structure is also seen in 8.4 GHz global geodetic VLBI images of PKS 0537–441, which are almost resolution-matched to the VSOP image (§ 2.2).

3.4. PKS 0637–752

PKS 0637–752 was first imaged with VLBI by Tingay et al. (1998c) at 5 GHz with 2 mas angular resolution. The ground-based image shows a bright core component and a jetlike extension to the west of approximately 5 mas length, which consists of several components. Figures 2 and 3 show our two images of this source, at 4.976 and 4.816 GHz, showing in greater detail the components within 3 mas of the core. Table 3 lists the core parameters from the first epoch of data (Fig. 2); the core parameters from the second epoch gave a brightness temperature estimate very consistent with the first-epoch data. These two observations were approximately 20 months apart, and changes in the structure of the jet are apparent in that time, although one needs to be wary of the effects due to the different (u, v) coverages. These images have already been discussed elsewhere in conjunction with geodetic VLBI images, ATCA observations, *Hubble Space Telescope* observations, and the first astronomical observations of the *Chandra X-Ray Telescope* (Schwartz et al. 2000; Chartas et al. 2000; Lovell et al. 2000b). Briefly, the VSOP and geodetic VLBI data yield proper motions of 0.41 ± 0.03 , 0.29 ± 0.05 , and 0.36 ± 0.09 mas yr $^{-1}$ for three components in the jet. The proper motions are just consistent with a weighted average apparent speed of $(17.8 \pm 1.0)c$ ($H_0 = 70$ km s $^{-1}$ and $q_0 = 0.15$; Schwartz et al. 2000; Lovell et al. 2000b).

3.5. PKS 1104–445

PKS 1104–445 was included in the first southern hemisphere VLBI Experiment observations (Preston et al. 1989); from limited data (13 mas angular resolution) they model the source as a 2.5 Jy, 4 mas FWHM Gaussian component with a 0.2 Jy pointlike secondary component approximately 17 mas away at a position angle of approximately 75° . Shen et al. (1997) imaged PKS 1104–445 at 5 GHz with a global array (3 mas angular resolution) and found a 1.79 Jy core and evidence for jet components within 3 mas of the core between position angles of 41° and 62° . Our VSOP data are consistent with previous observations on the Earth baselines but show the source to be heavily resolved on baselines greater than $300 M\lambda$ at 5 GHz, leaving a compact component of 0.3 Jy on the longest space baselines (Fig. 3).

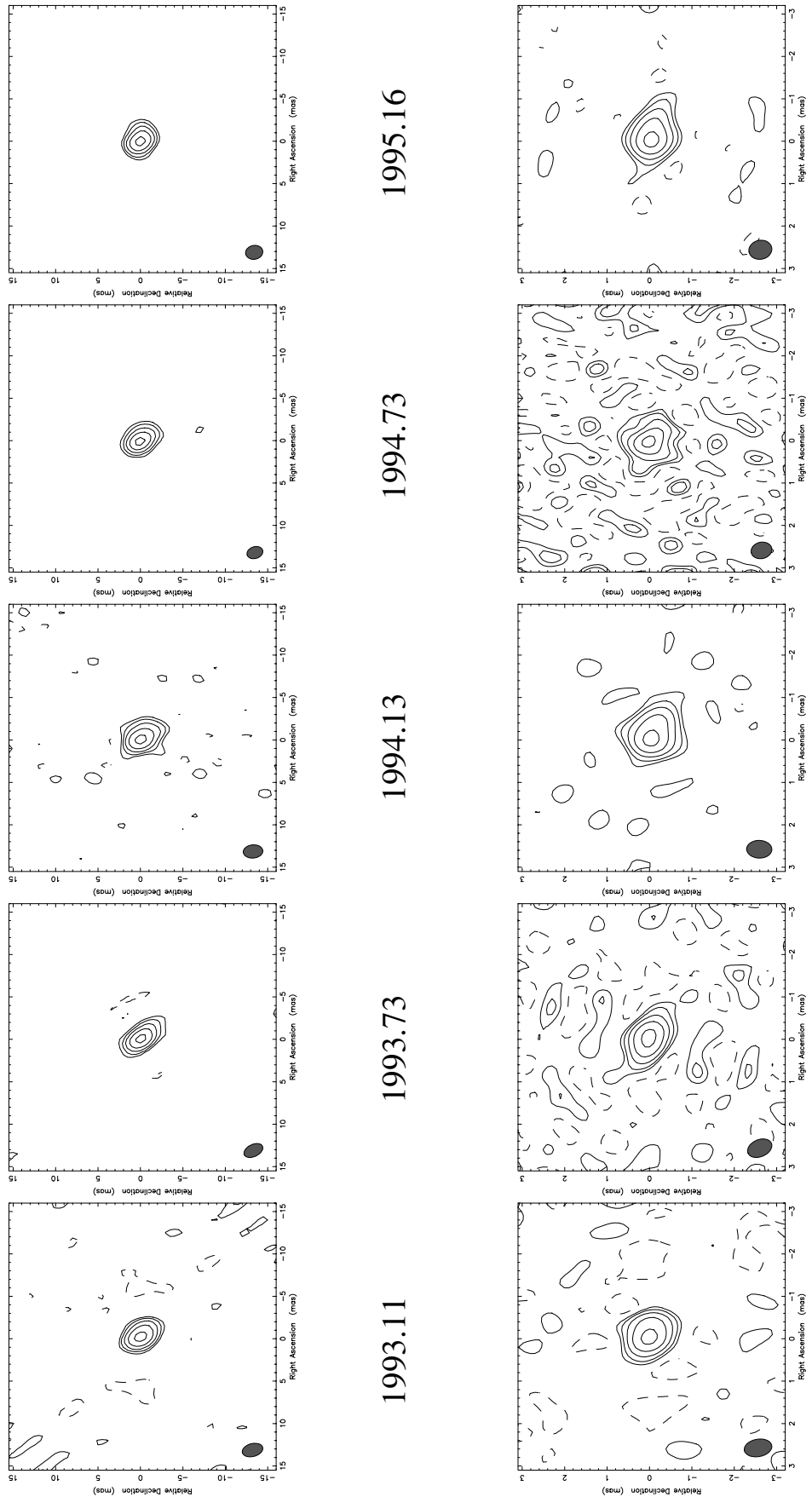


FIG. 12.—Geodetic images of PKS 0208—512. *Top*: Sequence of five images at 2.3 GHz. *Bottom*: Sequence of five images at 8.4 GHz. The lowest contours for all images are 4%, and the highest contours are 64% of peak brightness. Peak brightness can be inferred from the model-fit flux densities of Table 5.

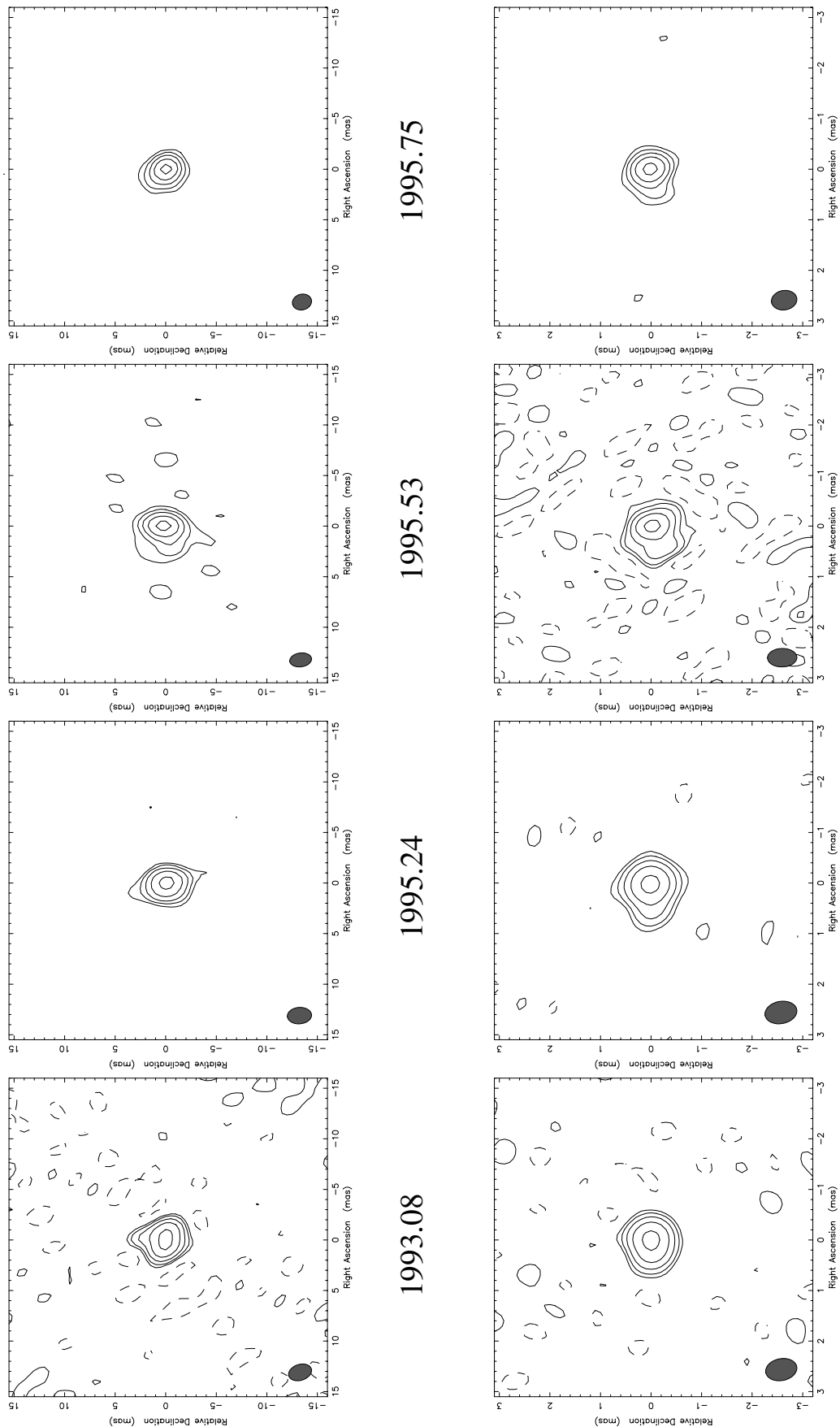


FIG. 13.—Geodetic images of PKS 0537–441. *Top*: Sequence of four images at 2.3 GHz. *Bottom*: Sequence of four images at 8.4 GHz. The lowest contours for all images are 4%, and the highest contours are 64% of peak brightness. Peak brightness can be inferred from the model-fit flux densities of Table 6.

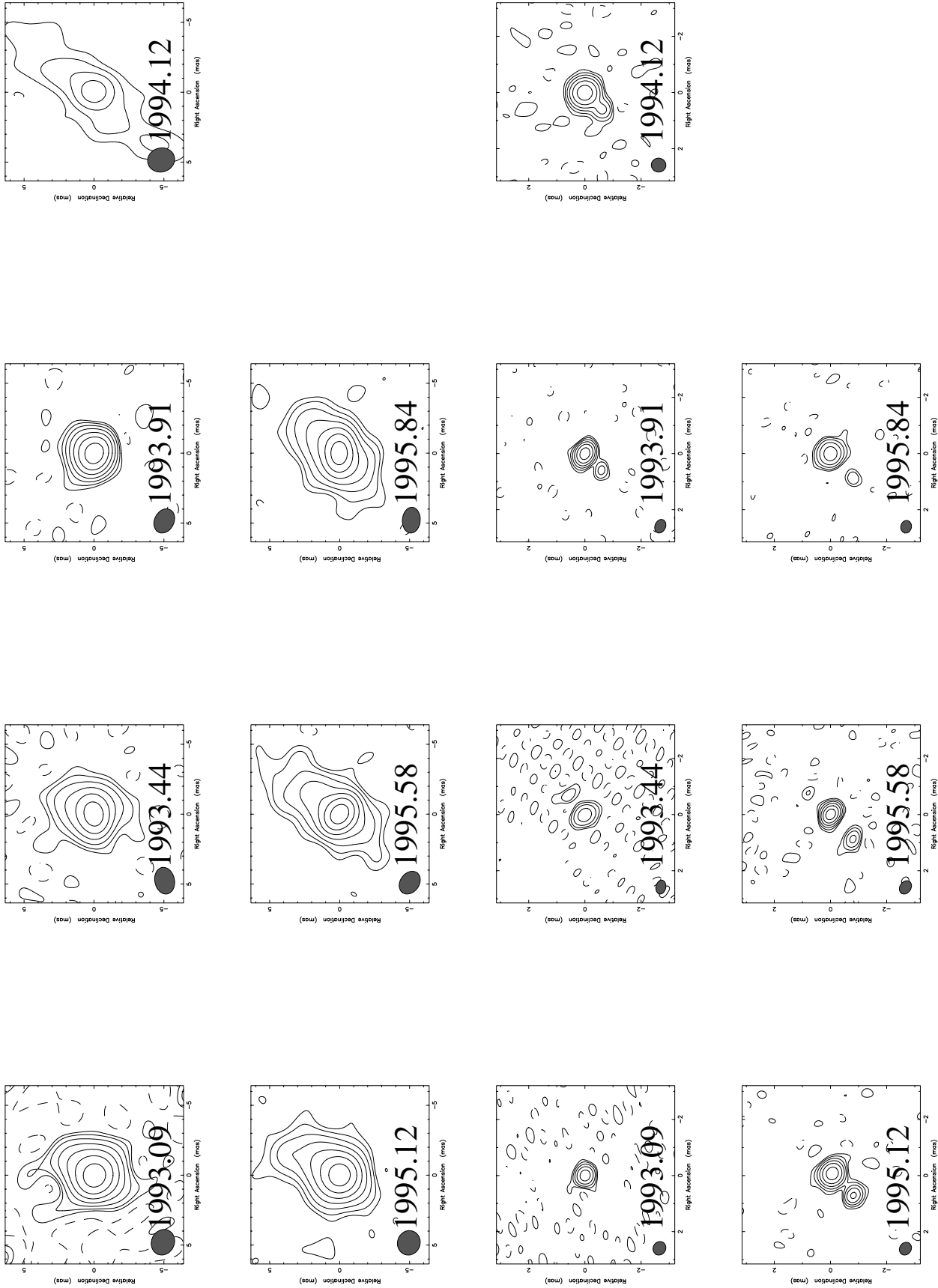


FIG. 14.—Geodetic images of PKS 1610–771. *Top*: Sequence of seven images at 2.3 GHz. The lowest contours for the 2.3 GHz images, in temporal order, are 1%, 2%, 1%, 8%, 1%, 1%, and 1%, and the highest contours are 64% of peak brightness. Peak brightness can be inferred from the model-fit flux densities of Table 7. *Bottom*: Sequence of seven images at 8.4 GHz. The lowest contours for the 8.4 GHz images, in temporal order, are 4%, 8%, 2%, 2%, 2%, 2%, and 4%, and the highest contours are 64% of peak brightness. Peak brightness can be inferred from the model-fit flux densities of Table 7.

TABLE 5
GEODETIC VLBI MODELS FOR PKS 0208–512

Date	S	R	θ (deg)	a
2.3 GHz				
1993.11	1.6	0.0	0	0.5
	1.1	1.3	-119	0.4
1993.73	1.9	0.0	0	0.8
	0.7	1.3	-128	0.9
1994.13	1.9	0.0	0	0.2
	1.6	1.4	-133	1.3
1994.73	2.9	0.0	0	0.7
	1.9	1.1	-134	1.4
1995.16	2.8	0.0	0	0.9
	0.4	1.3	-122	0.0
8.4 GHz				
1993.11	2.4	0.0	0	0.5
1993.73	2.5	0.0	0	0.5
1994.13	3.0	0.0	0	0.5
	0.6	0.7	-114	0.1
1994.73	3.2	0.0	0	0.4
1995.16	2.4	0.0	0	0.4
	0.4	0.7	-108	0.2

NOTE.—Cols. (2)–(5) are as for Table 3.

3.6. PKS 1127–145

PKS 1127–145 is a well-studied quasar that has been investigated with VLBI by several authors at frequencies between 1.7 and 22 GHz (Jorstad et al. 2001; Tingay et al. 1998a; Shen et al. 1998; Kellermann et al. 1998; Fey, Clegg, & Fomalont 1996; Bondi et al. 1996; Wehrle et al. 1992; Linfield et al. 1989, 1990). The source basically consists of a strong east-west double plus a weak extension to the north-east (Wehrle et al. 1992) and complicated emission between the double components (Jorstad et al. 2001). Linfield et al. (1989, 1990) detected PKS 1127–145 on 14,000 km space VLBI baselines using the *TDRSS* satellite as the orbiting

TABLE 6
GEODETIC VLBI MODELS FOR PKS 0537–441

Date	S	R	θ (deg)	a
2.3 GHz				
1993.08	3.5	0.0	0	2.1
1995.24	3.5	0.0	0	1.0
1995.53	4.2	0.0	0	1.4
1995.75	3.6	0.0	0	1.4
8.4 GHz				
1993.08	2.6	0.0	0	0.3
	0.5	0.4	95	0.1
1995.24	4.2	0.0	0	0.1
	2.3	0.5	88	0.7
1995.53	5.5	0.0	0	0.2
	1.5	0.5	117	0.0
1995.75	3.7	0.0	0	0.2
	1.1	0.4	90	0.2

NOTE.—Cols. (2)–(5) are as for Table 3.

TABLE 7
GEODETIC VLBI MODELS FOR PKS 1610–771

Date	S	R	θ (deg)	a	b/a	ϕ (deg)
2.3 GHz						
1993.09	0.7	0.14	103	0	1	0
	1.0	0.31	-74	2.7	0.6	-23
1993.44	1.2	0.04	116	0	1	0
	2.1	0.41	-38	3.0	0.7	-6
1993.91	1.2	0.01	129	0.7	0.7	-44
	0.1	1.3	-37	0	1	0
1995.12	1.1	0.06	175	0	1	0
	1.6	0.53	-27	3.2	0.6	-37
	0.1	4.1	-22	0	1	0
1995.58	1.5	0.01	-163	0	1	0
	1.6	0.76	-33	5.0	0.4	-36
1995.84	1.5	0.02	-23	0	1	0
	2.3	0.24	-23	4.0	0.5	-46
8.4 GHz						
1993.09	0.5	0.0	0	0	1	0
1993.44	1.7	0.0	115	0.4	1	0
	0.2	0.8	135	0	1	0
1993.91	0.9	0.0	74	0.2	1	0
	0.1	0.8	135	0	1	0
1994.12	2.5	0.0	54	0.4	1	0
	0.3	0.9	135	0	1	0
1995.12	1.7	0.0	-132	0.3	1	0
	0.4	1.1	138	0	1	0
1995.58	0.8	0.0	-130	0	1	0
	0.2	1.2	132	0	1	0
1995.84	1.9	0.0	-47	0.4	1	0
	0.2	1.2	132	0	1	0

NOTE.—Cols. (2)–(7) are as for Table 3.

element, at both 2.3 and 15 GHz. Vermeulen & Cohen (1994) listed a proper motion of 0.00 ± 0.02 mas yr⁻¹ in their compilation of proper motion statistics. The 22 GHz monitoring of Jorstad et al. (2001) clarifies the situation somewhat; they measure stationary and moving components ranging up to $(19.8 \pm 6.1) h^{-1}c$.

Our VSOP image (Fig. 4) shows the structure that is consistent with previously published ground-based images; a strong double with a northeast extension and emission between the double components. Figure 4 is annotated with the component designations from Jorstad et al. (2001), which are discussed below.

The brightness temperature of the presumed core (at the western end of the source), component A (Jorstad et al. 2001), is listed in Table 3.

To investigate the motions of components in PKS 1127–145, we have compiled all VLBI observations of PKS 1127–145 from the literature, at different frequencies (Jorstad et al. 2001; Tingay et al. 1998b; Shen et al. 1998; Kellermann et al. 1998; Fey et al. 1996; Bondi et al. 1996; Wehrle et al. 1992), to produce an overall temporal history of the milliarcsecond-scale component positions in this source, shown in Figure 16. Included in this compilation are the VSOP data from this work. We have adopted errors from the literature where given, or half the beam size where errors have not been given. For the VSOP data, we measured the positions of components in the image plane in DIFMAP and adopted the full beam size as the error, in rec-

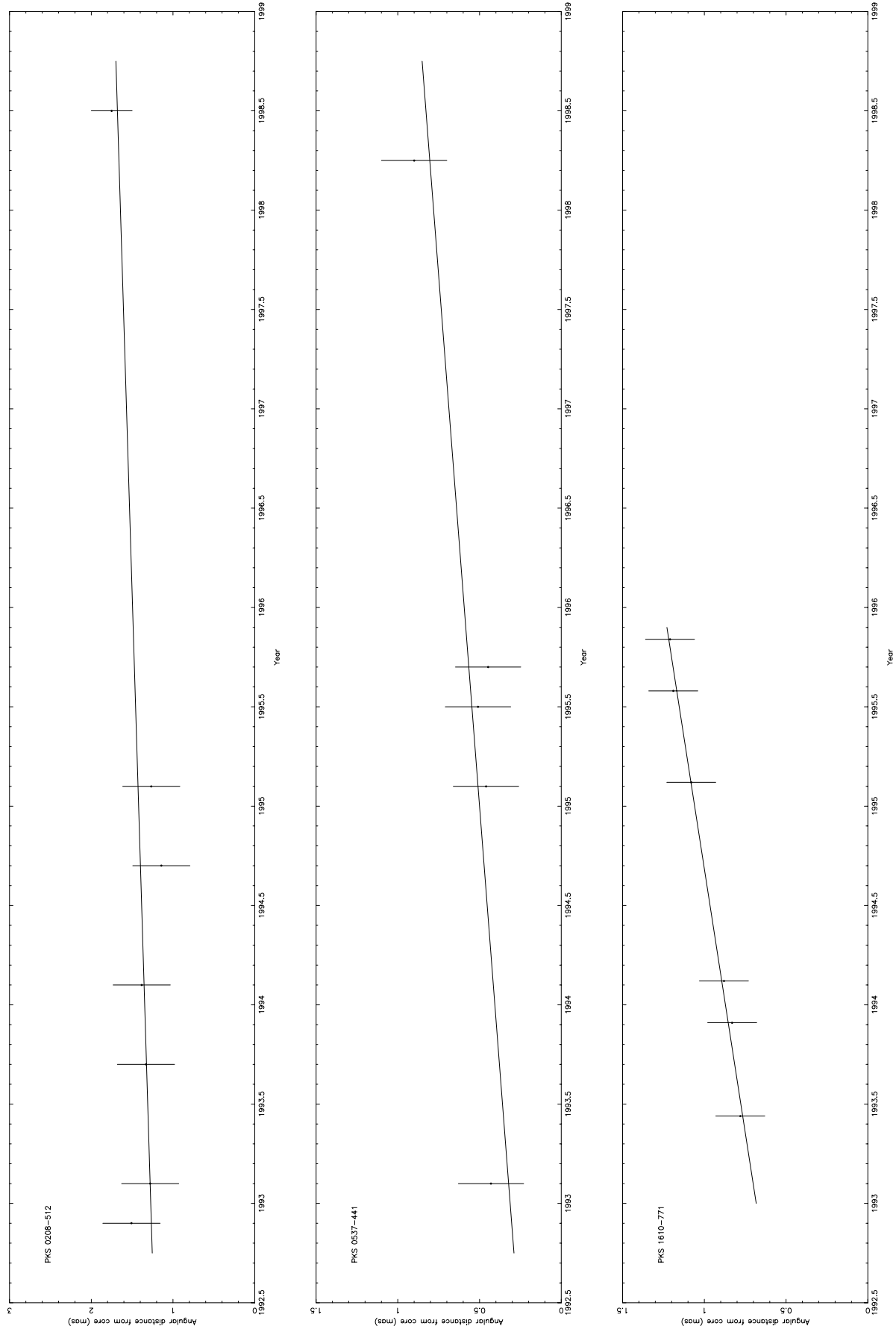


Fig. 15.—Core-component separations as a function of time and linear least-squares fits for the apparent proper motions in PKS 0208–512 (*top*), PKS 0537–441 (*middle*), and PKS 1610–771 (*bottom*), from the geodetic and VSOP data sets.

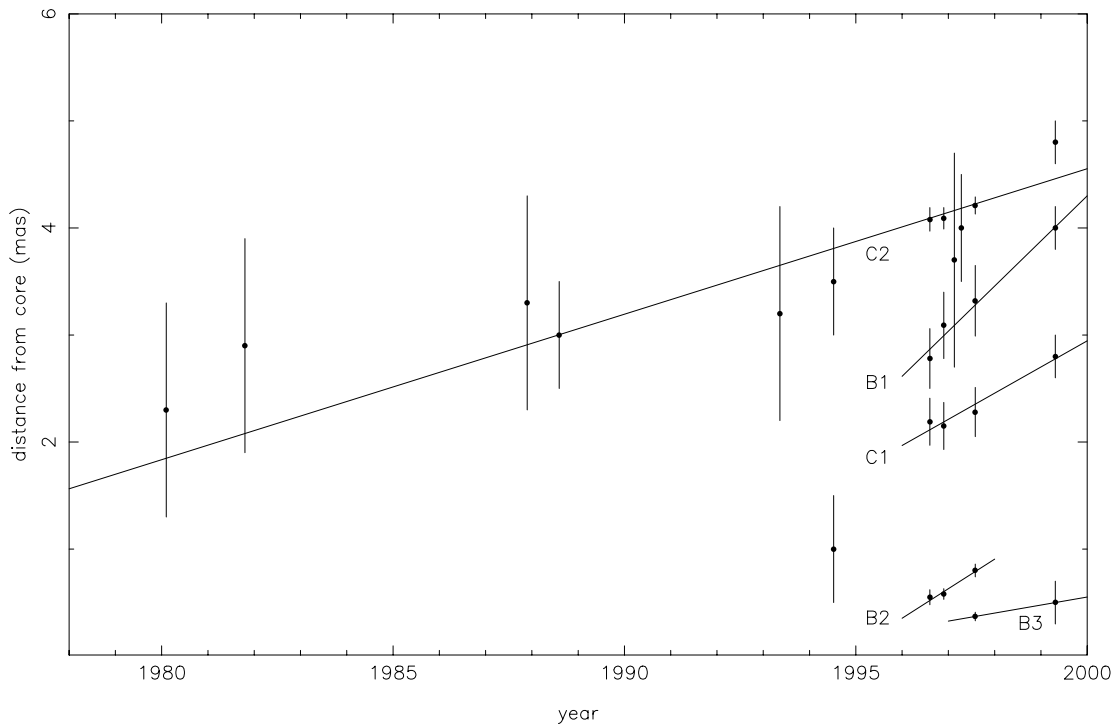


FIG. 16.—Positions of milliarcsecond-scale components in PKS 1127–145 relative to the core component, as a function of time, compiled from the literature and this work. Component designations are from Jorstad et al. (2001). Solid lines are weighted linear least-squares fits to the data.

ognition of the sparse (u, v) coverage of the VSOP data. In Figure 16 the VSOP data are the points at 1999.31.

Observations of PKS 1127–145 prior to 1994 were model-fitted with a two-component model at 1.6 GHz (Bondi et al. 1996; 1980.10, 1981.80, and 1987.90) and 5.0 GHz (Shen et al. 1998; 1993.36). In Figure 16 these two components are taken to be dominated by components A (the core) and C2. The 5.0 GHz image of Wehrle et al. (1992; 1988.59) was not model-fitted, but the two components are clearly resolved, allowing an estimate of the component separation from the published image. Likewise, the 8.6 GHz image of Fey et al. (1996; 1994.52) is well resolved, showing the two components; however, Fey et al. (1996) provide model-fit positions for these components, which have been used in Figure 16. The identification for the component 1 mas from the core at 1994.52 (Fey et al. 1996) is unclear.

The VSOP image in Figure 4 has detected components A, B1, B3, C1, and C2 at 1999.31. The positions of these components derived from the VSOP data generally fit well into the overall picture of an expanding jet source. The fact that component B2 was not detected is interesting, but it can be noted that Jorstad et al. (2001) previously observed another component, D1, emerge from the core and fade to below the noise level at approximately the same position that B2 appears to have faded. Even though Figure 16 contains position estimates at a number of different frequencies and resolutions, which should prompt caution in such a comparison, there appears to be good evidence that all milliarcsecond-scale components in PKS 1127–145 are moving away from the core.

The weighted linear least-squares fit to the compiled data for component B1 gives a proper motion of 0.42 ± 0.08 mas yr^{-1} , corresponding to $\beta_{\text{app}} = (16.0 \pm 3.0) h^{-1}$, not signifi-

cantly different from that found by Jorstad et al. (2001). The high signal-to-noise points from the 22 GHz monitoring of Jorstad et al. (2001; 1996.60, 1996.90, 1997.58) dominate the weighted linear least-squares fit to the C2 component positions, shown in Figure 16. The 15 GHz image of Kellermann et al. (1998; 1997.28) and the 8.4 GHz image of Tingay et al. (1998b; 1997.13) are consistent with the Jorstad et al. (2001) data for C2. The VSOP data and historical data from the literature indicate that components C1 and C2 have apparent proper motions of 0.24 ± 0.10 and 0.14 ± 0.06 mas yr^{-1} , corresponding to $\beta_{\text{app}} = (9.1 \pm 3.8) h^{-1}$ and $\beta_{\text{app}} = (5.3 \pm 2.3) h^{-1}$, respectively (over the course of almost 20 yr for C2). Previously Jorstad et al. (2001) suggested that C1 and C2 are stationary components, based on three 22 GHz observations over a period of 1 yr.

The estimate of 0.27 ± 0.05 mas yr^{-1} for component B2, corresponding to $\beta_{\text{app}} = (10.3 \pm 1.9) h^{-1}$, from Jorstad et al. (2001) remains unchanged. Finally, from two epochs of data, the proper motion for component B3 is 0.08 ± 0.13 mas yr^{-1} , corresponding to $\beta_{\text{app}} = (3.0 \pm 4.9) h^{-1}$.

Further high-frequency and high-resolution VLBI monitoring is required to confirm the motions of all milliarcsecond-scale components in PKS 1127–145.

3.7. PKS 1424–418

PKS 1424–418 was modeled by Preston et al. (1989) as a 1.4 Jy core and a 0.26 Jy secondary component a distance of 23 mas from the core at a position angle of 56° , from 2.3 GHz VLBI with an angular resolution of 13 mas. Shen et al. (1998) imaged the source at 5 GHz with 2 mas resolution and found a 1.36 Jy core with a 0.12 Jy secondary, 2.74 mas distant at a position angle of 260° . Our VSOP image (Fig. 4) shows a compact component with a jetlike extension at a

position angle close to the position angle noted by Preston et al. (1989).

3.8. *PKS 1610–771*

There are no detailed ground-based VLBI observations of PKS 1610–771 in the previous literature. Preston et al. (1989) modeled the source as a 3.8 Jy component 10 mas in extent with a 1.4 Jy halo approximately 50 mas in diameter, using data with 22 mas resolution. Our VSOP data confirm the presence of a very extended component detected only on Earth baselines. However, the small-scale structure is resolved into three components at a position angle of approximately -30° (Fig. 5). Table 3 lists the southern component, which is the brightest and most compact component detected, but it is not necessarily the core. The interpretation of the dual-frequency geodetic data of § 2.2 is consistent with this component being the stationary core component.

Comparison of the geodetic data and the VSOP data indicate a complicated variable, evolving, expanding structure with different spectral components.

3.9. *PKS 1622–253*

PKS 1622–253 has previously been imaged with VLBI by Fey et al. (1996) at 2.3 and 8.4 GHz (9 and 3 mas resolution, respectively), Tingay et al. (1998a) at 4.8 GHz (2 mas resolution), and Jorstad et al. (2001) at 22 GHz (0.8 mas resolution). From the ground-based images of Tingay et al. (1998c) and Jorstad et al. (2001) a strong core and weak jet-like extension is evident, along position angle $\sim 300^\circ$. Jorstad et al. (2001) have measured the apparent speed of this jetlike extension to be $\beta_{\text{app}} = (14.1 \pm 3.6) h^{-1}$. Our VSOP image (Fig. 5) shows that the core component is marginally resolved. The extended jet is completely resolved in the VSOP image but detected on the Earth baselines. PKS 1622–253 has been shown to display intraday variability (Bignall et al. 2002).

3.10. *PKS 1622–297*

PKS 1622–297 is the most luminous (assuming isotropic emission) gamma-ray source ever detected (Mattox et al. 1997) and has previously been imaged with VLBI at 1.7 and 5.0 GHz by Tingay et al. (1998a) and at 15, 22, and 43 GHz by Jorstad et al. (2001). The ground-based images at all frequencies are consistent and show a series of components along a position angle of -69° . Jorstad et al. (2001) find a weak stationary feature 15.4 mas from the nucleus at 15 GHz (which is stronger in the 5.0 GHz image of Tingay et al. 1998b). Jorstad et al. (2001) also find components at 3 and 5 mas from the core that have apparent speeds of $10 h^{-1}c$ and components within 1.5 mas with apparent speeds between 5 and $10 h^{-1}c$. The VSOP image (Fig. 6) of PKS 1622–297 shows a strong core and a weaker component approximately 1.5 mas from the core, consistent with the position of component D1 identified from the 22 GHz monitoring of Jorstad et al. (2001); much weaker jet structure is apparent farther from the core, close to the jet position angle of -69° . PKS 1622–297 has also been shown to display intraday variability (Bignall et al. 2002). An ATCA image of PKS 1622–297 at 4.8 GHz reveals a bright core with strong extended emission in the form of two components, placed equal angular distances either side of the core ($7''$) with similar sizes and brightnesses, along a position

angle of 22° , almost exactly 90° offset from the VLBI jet position angle (S. J. Tingay & B. Punsly 2002, in preparation). This extended structure was first noted by Perley (1982).

3.11. *PKS 1718–649*

PKS 1718–649 is the lowest redshift GHz-peaked spectrum radio source (Tingay et al. 1997). The radio structure is approximately 7 mas in total extent and, as is typical for GPS galaxies, consists of two almost equally bright components. The VSOP data we obtained for this source are sparse and could not be easily imaged, probably because the combination of sparse (u, v) coverage and highly resolved structure (§ 2) is not well suited to the clean algorithm. However, a good model fit was possible (Fig. 6) and shows that the two components are resolved on space baselines. The ground-based images of Tingay et al. (1997) and the space VLBI model agree extremely well. The measured separation of the two components has remained the same (approximately 7 mas), to within the errors (approximately 0.5 mas) over a period of 6 yr, implying an upper limit on the separation speed of the components of $0.08c$ [cf. $(0.05 \pm 0.2)c$ for PKS 1934–638, another low-redshift GPS galaxy (Tzioumis et al. 1989)]. Since both components in PKS 1718–649 are similar in brightness temperature and neither is likely to be the nucleus, both components are listed in Table 3. Typically the core components in GPS sources are very weak. A higher sensitivity (and possibly higher frequency) VLBI observation would be required to detect the core component in PKS 1718–649.

3.12. *PKS 2152–699*

PKS 2152–699 is a low-redshift Fanaroff-Riley type II radio galaxy with strong nuclear radio emission. The nuclear radio source has been investigated with VLBI, and its relationship to the larger scale radio and optical structure of the galaxy has been discussed (Tingay et al. 1996b). The VSOP image (Fig. 7) shows a resolved core and highly linear, narrow jet approximately 6 mas in extent. The position angle of the jet is in excellent agreement with that found by Tingay et al. (1996b).

3.13. *PKS 2255–282*

PKS 2255–282 came to attention as a flaring gamma-ray source (Bertsch et al. 1998). Tornikoski et al. (1999) published multiwavelength data, including ground-based VLBI, for this quasar. The VLBI image of Tornikoski et al. (1999; 3 mas resolution) shows a strong core component and a jet extending approximately 5 mas to the southwest. Our VSOP image (Fig. 7) shows the strong core component; the extended jet is heavily resolved, although weakly apparent in the image.

3.14. *PKS 2355–534*

The 5 GHz VLBI observations of Shen et al. (1998; 3 mas resolution) show PKS 2355–534 to have two components, of 1.54 and 0.20 Jy, of equal size and separated by 4.88 mas. Our VSOP data proved insufficient to produce an image. Figure 8 shows a single-component model fit of the data, which appears in Table 3.

4. CONCLUSIONS

We have presented the highest resolution images and model fits yet for the majority of the 14 southern hemisphere compact radio sources investigated here. Model-fitting of the most compact components of these sources (in most cases corresponding to the core) show that the two low-redshift radio galaxies PKS 1718–649 (GHz-peaked spectrum) and PKS 2152–699 (FR II) have the lowest peak brightness temperatures, as expected since neither are likely to be highly Doppler boosted. However, the two galaxies are less luminous and closer than the quasars in the sample and in PKS 1718–649 we have not likely detected the core component. Therefore, factors other than differences in Doppler boosting may cause the brightness temperatures of the galaxies to be systematically lower than for the quasars.

Of the sources optically identified as quasars, six have been detected in greater than 100 MeV gamma rays by the EGRET instrument aboard the *CGRO* and six have not been detected by EGRET. One of the chief goals of these VSOP observations was to compare the properties of EGRET-identified and gamma-ray-quiet AGNs (see discussion in Tingay et al. [1996a, 1998a, 1998b, 1998c]); to see why such a comparison is interesting). The sample of gamma-ray-loud sources can be considered close to a flux density limited (at gamma-ray energies) sample, while the gamma-ray-quiet sources have been selected to be representative of the parent population of gamma-ray-loud sources, based on radio and optical properties. From Table 3 and Figure 9, a comparison of the brightness temperature distributions for these two classes of source shows no obvious differences; a range in observer's frame brightness temperature between approximately 1.0×10^{12} and 1.2×10^{12} K is consistent with the measurements for all of the quasars and likewise, in the source frame, brightness temperatures between approximately 2.0×10^{12} and 3.3×10^{12} K are consistent with all sources. These results are consistent with those of Tingay et al. (2001) and Lister et al. (2001b), who found no differences in source frame brightness temperatures between EGRET-identified and gamma-ray-quiet AGNs from a study of the Pearson-Readhead VLBI sample using the VSOP facilities.

Also, considering the quasars, we find no evidence for relationships between VSOP-derived brightness temperatures and average values of the radio flux density, spectral index, percentage polarization, and variability index as tabulated in Table 2 (and shown graphically in Figure 17). This was also the case when considering the measurements of these parameters taken closest in time to each VSOP observation, rather than considering average values. The small number of sources to consider and the abundance of only lower limits in the data may make the detection of significant correlations between VSOP-derived brightness temperature and other parameters difficult; a full statistical analysis of these data, similar to that performed by Lister et

al. (2001b), will appear elsewhere. However, the lack of obvious correlation agrees with the results of Lister et al. (2001b), who, in a full statistical analysis of a better defined, larger, and more complete sample of sources, found that VSOP-derived brightness temperatures did not correlate with any standard indicators of relativistic beaming, only intraday variability (IDV). The conclusion of Lister et al. (2001b) was that IDV was also correlated with relativistic beaming indicators such as radio spectral index, optical emission line equivalent width, and source size. The interpretation of this conclusion is complicated by the fact that most IDV is thought to be caused by a mechanism extrinsic to the source, scintillation due to a screen of material between the source and observer (e.g., Bignall et al. 2002). Although some of the southern objects described in this paper are known IDV sources, overall there are not enough IDV monitoring observations of the full sample to perform a test similar to that done by Lister et al. (2001b).

In terms of variability, three of the gamma-ray-loud quasars (PKS 0537–441, PKS 1622–253, and PKS 2255–282) are far more variable (Table 1 and Fig. 17) than the other sources. PKS 0537–441 and PKS 1622–253 are known as probable IDV sources and the variability may be due in part to interstellar scintillation rather than intrinsic mechanisms. While not significant in such a small sample, analysis of the full ATCA monitoring database should be undertaken to determine whether there is a significant difference in the variability properties of gamma-ray-loud and gamma-ray-quiet AGNs. PKS 2255–282 also has by far the most inverted radio spectrum of all the sources.

The VSOP work reported here has been particularly useful in analyses of the structural evolution of five sources, PKS 0208–512, PKS 0537–441, PKS 0637–752 (Schwartz et al. 2000; Chartas et al. 2000; Lovell et al. 2000b), PKS 1127–145, and PKS 1718–649. Geodetic VLBI data have also proved extremely useful in these investigations.

We gratefully acknowledge the VSOP Project, which is led by the Japanese Institute of Space and Astronautical Science in cooperation with many organizations and radio telescopes around the world. The Australia Telescope is funded by the Australian Commonwealth Government for operation as a national facility managed by CSIRO. Part of this work was undertaken at the Jet Propulsion Laboratory, California Institute of Technology, under contract with the National Aeronautics and Space Administration while S. J. T. held an NRC/NASA-JPL Research Associateship. The Astronomical Image Processing Software (AIPS) and the VLBA were developed and are maintained by the National Radio Astronomy Observatory, which is operated by Associated Universities, Inc., under cooperative agreement with the National Science Foundation. We thank the appointed referee, Ed Fomalont, for a careful review of the manuscript and suggestions that improved the paper.

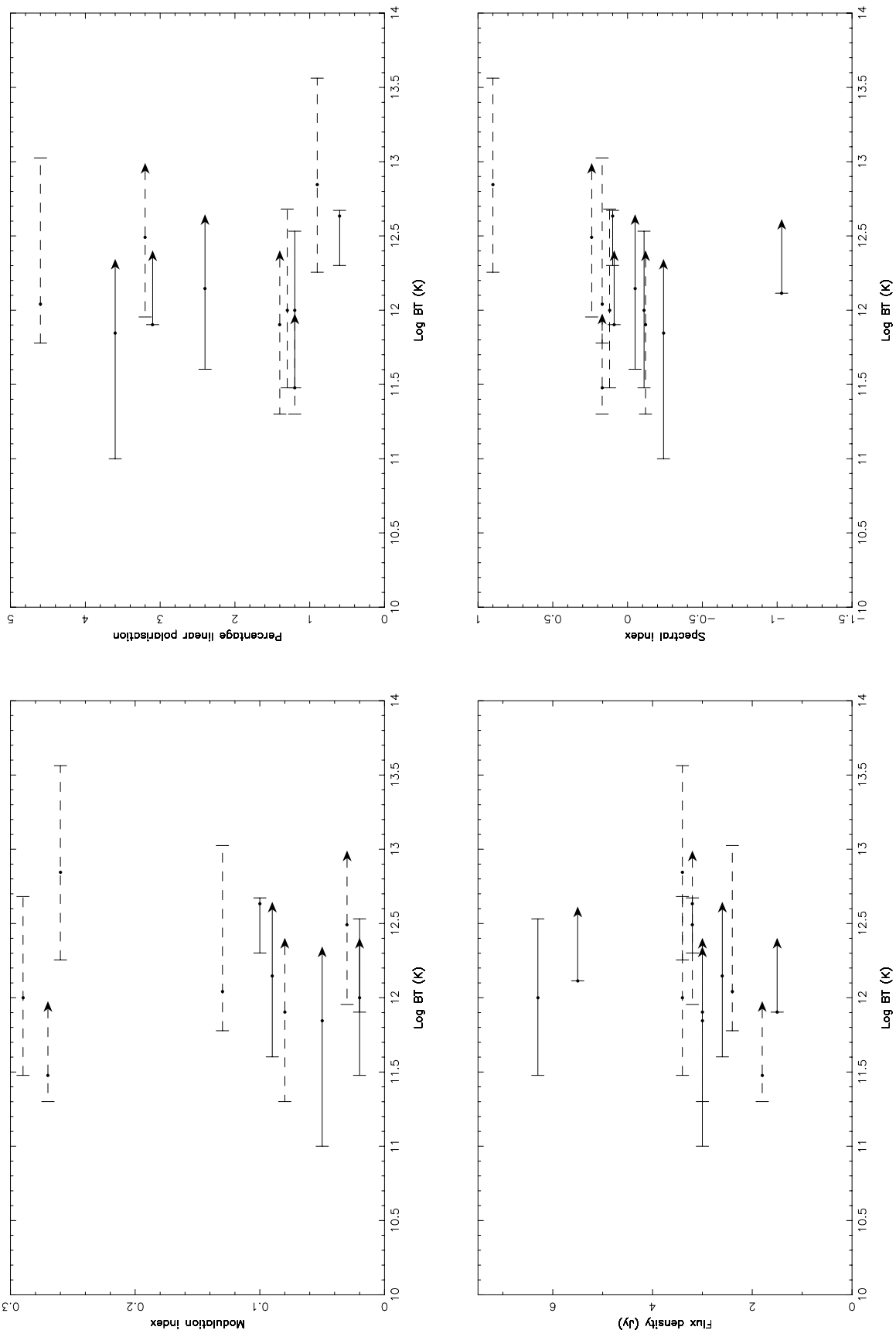


Fig. 17.—Plots of quantities derived from ATCA monitoring observations for the quasars (modulation index, percentage linear polarization, flux density, and spectral index) against VSP0P-derived brightness temperatures. ATCA data are described in the text and tabulated in Table 1. The EGRET-identified quasars are represented by the dashed lines and the gamma-ray-quiet quasars by the solid lines.

REFERENCES

- Bertsch, D., et al. 1998, IAU Circ. 6807
Bignall, H. E., et al. 2002, Publ. Astron. Soc. Australia, 19, 29
Bondi, M., et al. 1996, A&A, 308, 415
Chartas, G., et al. 2000, ApJ, 542, 655
Fey, A. L., Clegg, A. W., & Fomalont, E. B. 1996, ApJ, 468, 543
Fichtel, C. E., et al. 1994, ApJS, 94, 551
Hartman, R. C., et al. 1999, ApJS, 123, 79
Hirabayashi, H., et al. 1998, Science, 281, 1825
———. 2000a, PASJ, 52, 955
———. 2000b, PASJ, 52, 997
Jorstad, S. G., Marscher, A. P., Mattox, J. R., Wehrle, A. E., Bloom, S. D., & Yurchenko, A. V. 2001, ApJS, 134, 181
Kellermann, K. I., Vermeulen, R. C., Zensus, J. A., & Cohen, M. H. 1998, AJ, 115, 1295
Linfield, R. P., et al. 1989, ApJ, 336, 1105
———. 1990, ApJ, 358, 350
Lister, M. L., Tingay, S. J., & Preston, R. A. 2001b, ApJ, 554, 964
Lister, M. L., Tingay, S. J., Murphy, D. W., Piner, B. G., Jones, D. L., & Preston, R. A. 2001a, ApJ, 554, 948
Lovell, J. E. J., et al. 2000a, in *Astrophysical Phenomena Revealed by Space VLBI*, ed. H. Hirabayashi, P. G. Edwards, & D. W. Murphy (Sagamihara: ISAS), 183
———. 2000b, in *Astrophysical Phenomena Revealed by Space VLBI*, ed. H. Hirabayashi, P. G. Edwards, & D. W. Murphy (Sagamihara: ISAS), 215
———. 2000c, in *Astrophysical Phenomena Revealed by Space VLBI*, ed. H. Hirabayashi, P. G. Edwards, & D. W. Murphy (Sagamihara: ISAS), 301
Mattox, J. R., et al. 1997, ApJ, 476, 692
Moellenbrock, G. A., et al. 2000, in *Astrophysical Phenomena Revealed by Space VLBI*, ed. H. Hirabayashi, P. G. Edwards, & D. W. Murphy (Sagamihara: ISAS), 183
Murphy, D. W., et al. 1993, in *Subarcsecond Radio Astronomy*, ed. R. J. Davis & R. S. Booth (Cambridge: Cambridge Univ. Press), 243
Perley, R. A. 1982, AJ, 87, 859
Piner, B. G., & Kingham, K. A. 1998, ApJ, 507, 706
Preston, R. A., et al. 1989, AJ, 98, 1
Schwartz, D. A., et al. 2000, ApJ, 540, 69
Shen, Z.-Q., et al. 1997, AJ, 114, 1999
———. 1998, AJ, 115, 1357
Shepherd, M. C., Pearson, T. J., & Taylor, G. B. 1994, BAAS, 26, 987
Stickel, M., Meisenheimer, K., & Kühr, H. 1994, A&AS, 105, 211
Tateyama, C. E., Kingham, K. A., Piner, B. G., de Lucena, A. M. P., & Botti, L. C. L. 1999, ApJ, 520, 627
Tingay, S. J., et al. 1996a, ApJ, 464, 170
———. 1996b, AJ, 111, 718
———. 1997, AJ, 113, 2025
———. 1998a, AJ, 115, 960
Tingay, S. J., Murphy, D. W., & Edwards, P. G. 1998b, ApJ, 500, 673
———. 1998c, ApJ, 497, 594
———. 2000, AJ, 119, 1695
———. 2001, ApJ, 549, L55
Tornikoski, M., et al. 1999, AJ, 118, 1161
Tzioumis, A. K., et al. 1989, AJ, 98, 36
Vermeulen, R. C., & Cohen, M. H. 1994, ApJ, 430, 467
Wehrle, A. E., et al. 1992, ApJ, 391, 589